SAPIENZA
UNIVERSITÀ DI ROMA

Search for *R*-Mode Gravitational Signals from PSR J0537-6910

Facoltà di Scienze Matematiche, Fisiche e Naturali

Corso di Laurea Magistrale in Fisica

Candidate

Alessio Zicoschi

ID number 1746313

Thesis Advisor

Dr. Cristiano Palomba

Co-Advisor

Dr. Simone Mastrogiovanni

Academic Year 2020/2021

Thesis defended on 19 July 2021
in front of a Board of Examiners composed by:

Prof. Ettore Majorana (chairman)
Prof. Franco Meddi
Prof. Cristiano De Michele
Prof. Stefano Giagu
Prof. Alfredo Urbano
Prof. Ernesto Placidi
Prof. Alessandro Paiella

Thesis Reviewer:

Prof. Irene Di Palma

Search for *R*-Mode Gravitational Signalsfrom PSR J0537-6910
Master's thesis. Sapienza – University of Rome

This thesis has been typeset by LaTeX and the Sapthesis class.

Version: July 9, 2021

Author's email: alessio.zicoschi@gmail.com

Dedicated to my family

Abstract

PSR J0537-6910 is a young (1-5 kyrs) energetic X-ray pulsar located in the Large Magellanic Cloud, which is known for its rather significant glitching activity (it is also known as *"The Big Glitcher"*). In 2020, the *NICER* telescope provided a detailed timing model for this pulsar overlapping the LIGO-Virgo O3 data-taking run. From these measurements, precise estimations for the pulsar rotational parameters and times of *glitch* occurrences are provided, which enabled an electromagnetically-triggered search. Moreover, measures of the pulsar *braking index* suggest that its *inter-glitch* value asymptotically relaxes towards a value of about 7. This points to the possibility the r-modes, which are a potentially interesting source of Continuous Gravitational Waves (CWs), are excited in this pulsar.

It is possible to perform a search for this kind of gravitational signals using an extension of the already tried-and-tested fully coherent narrow-band *5-vectors* pipeline, typically used to perform CWs searches for signals due to ellipticity. There are three main differences with respect to standard narrow-band searches, which need to be taken into account: the explored frequency band is ≈ 100 times larger ($\mathcal{O}(10\text{Hz})$ compared to $\mathcal{O}(10^{-1}\text{Hz})$ for ellipticity CWs), a fully coherent search cannot be performed due to the presence of *glitches*, and a different range of frequencies has to be explored for different spin-down rates. Thus the parameter space for this search is not a rectangle in the plane f-$\dot{f}$ (as in standard narrow-band searches), but it is a parallelogram. In fact, the underlying idea is to perform a coherent search over the different *inter-glitch* periods, and later incoherently combine the results. Thus, the overall search is semi-coherent.

This method has been applied to the search for r-mode gravitational emission from PSR J0537-6910 using data from the third LIGO-Virgo observing run. Unfortunately, it was not possible to claim a detection, since none of the candidates was significant enough. However, the search is indeed significantly more sensitive if compared to previous ones performed on the same target, and this is the first time that it was possible to account for *glitches* occurrences for this pulsar. Thus, it was possible to set interesting upper limits on the strain amplitude of an eventual signal: the obtained results not only are diving below the spin-down limit (defined by energy conservation) for relevant ranges of frequencies, but also allow us to set constraints on the theoretical models for r-modes, at least in the hypothesis that the pulsar spin-down is effectively driven by this kind of emission.

Therefore, it is possible to deduce that r-mode activity on this pulsar might be present, but the amplitude is lower than that needed to explain the observations of an *inter-glitch* braking index of $n = 7$. In particular, only scenarios where the pulsar mass is $M \lesssim 0.9 M_{\odot}$ and the star matter is described by a soft Equation of State are allowed. As an alternative, it is possible that r-modes are indeed excited by the *glitches*, but subsequently damped.

The results of this search are currently being published on *"The Astrophysical Journal"* and they are available on *arXiv* (2104.14417) under the title: *"Constraints from LIGO O3 data on gravitational-wave emission due to r-modes in the glitching pulsar PSR J0537-6910 "*.

Contents

Introduction

The existence of Gravitational Waves (GWs) was firstly derived by Albert Einstein in 1916 [1], just one year after his formulation of General Relativity. GWs are perturbations of the space-time metric which propagate at the speed of light. The most relevant contributions to the generation of gravitational waves are usually computed using a multipole expansion, which shows that the first relevant term is a time-changing quadrupole momentum in the mass-energy distribution of the studied physical system. Examples of physical systems characterized by a time-varying mass quadrupole are compact binary coalescing astrophysical systems (such as coalescing black holes or neutron stars) and spinning pulsars characterized by an unbalance in their axial mass distribution. However, the characteristic coupling constant associated with GWs is $G/c^4 \approx 8 \cdot 10^{-45}$ s^2/kg $\cdot$ m, which makes them very hard to detect. For this reason, it was necessary for the LIGO-Virgo Collaboration to put a lot of effort in order to achieve, after almost 50 years of work (and after exactly 100 years from Einstein's theoretical formulation), the first detection of a gravitational signal generated by a binary black hole coalescence: GW150914 [2].
The relevance of the detection of GWs is clear under many aspects: not only it proves the existence of this kind of waves (providing at the same time a confirmation of the theory of general relativity), but it also provides another channel (other than the electromagnetic one) to study astrophysical phenomena happening in the universe. For the latter reason, this detection marks the beginning of the *"multi-messenger astronomy"* era.
Since the first detection, the LIGO-Virgo Collaboration detected numerous transient gravitational signals originated by binary coalescences of different types. However, the theory of General Relativity predicts that there are systems (such as rotating non-axisymmetric pulsars) which in principle should generate detectable Continuous Gravitational Waves (CWs). Unfortunately, CWs have never been detected so far. A detection of this kind of waves would provide crucial information on the star structure and on the physics of matter in neutron stars, which is an interesting topic in modern physics. On one hand, the difficulty when dealing with CWs lies in the fact that their amplitude is much smaller than that of coalescences. On the other hand, CWs are expected to be detectable for a longer time, making it possible to perform coherent study over long data-taking time spans. For this reason, it becomes evident that the search for CWs is a particularly challenging task, as data analysis pipelines are based on complex algorithms usually requiring a huge amount of computational resources.
Another interesting possibility for the detection of CWs is represented by gravitational emission due to r-mode excitations. The r-mode is a toroidal mode of

oscillation of the pulsar fluid which is coupled to current-quadrupole GWs emissions. From an electromagnetic point of view, a possible candidate for r-mode activity is PSR J0537-6910 [3]. This pulsar is a young (1-5 kyrs) energetic X-ray pulsar located in the Large Magellanic Cloud at a distance of 49.6 kpc. From an astrophysical point of view, this pulsar is intriguing for several reasons: it is the fastest spinning young X-ray pulsar currently known ($\nu \approx 61.91\,\mathrm{Hz}$), it is the pulsar having the highest spin-down luminosity, and it exhibits large *glitches*, i.e., sudden decreases in spin frequency ($\Delta\nu/\nu \approx 10^{-7}$). In addition, PSR J0537-6910 *glitches* roughly every 100 days, while, in most pulsars, *glitches* do not happen regularly. Finally, this pulsar is unique, as it is the only glitching pulsar that shows a strong correlation between the size of a *glitch* and the waiting time to the next *glitch*, which suggests that a threshold level of some sort has to be reached to trigger the *glitch* mechanism.
The *NICER* telescope provided a detailed timing model for PSR J0537-6910 overlapping the LIGO-Virgo O3 run, that allows to perform the first electromagnetically triggered search for r-mode signals. In fact, previous searches (such as [4]) did not have the possibility to account for the presence of *glitches*, thus being partially incorrect, as the signal frequency evolution is modified by *glitches* occurrences. In addition, the *NICER* telescope measured an *inter-glitch braking index* n (defined as $n = \frac{\nu\ddot{\nu}}{\dot{\nu}^2}$, where ν is the pulsar rotational frequency and the dot indicates a time derivative) that relaxes towards a value of 7. This characteristic hints to the possibility that the energy is dissipated by the pulsar through gravitational emission due to r-modes.
Due to the present of *glitches*, it is not possible to perform a fully coherent search on the whole data-taking time span. In fact, when *glitches* occur, tha phase relation of the signal is not modeled. Thus, the search is split in two pieces: a fully coherent part, performed on different *inter-glitch* periods, and a part where results are incoherently combined.
This search was developed in the framework of the LIGO-Virgo collaboration using two independent pipelines: the Narrow-Band *5-Vectors* pipeline (developed in the Rome Virgo group) and the $\mathcal{F}/\mathcal{G}$ Statistic method (Virgo Polgraw group). The development of this search lead to the publication of the related LIGO-Virgo-KAGRA (LVK) Collaboration Paper [5].
I will begin this dissertation by describing, in Chapther 1 r-mode perturbations and how they are coupled to GWs emission. In particular, I will give a brief outline on CWs and on the emission parameters expected for an r-mode signal. I will then conclude this part with by presenting the timing model of PSR J0537-6910 obtained by the *NICER* telescope.
Moving on, in Chapter 2, I will describe how narrow-band CWs searches are usually performed. To do so, I will present the formalism of the coupling of GWs to interferometers, which is needed for the description of the workflow of the used pipeline. I will proceed by describing the most relevant steps of the narrow-band *5-vectors* pipeline and then I will discuss how this pipeline can be extended in order to be applied to r-mode searches.
Chapter 3 will be devoted to the incoherent combination of the results obtained in *inter-glitch* periods: this is a fundamental step for performing this r-mode search and it represents the main extension to the previously-used pipeline. I will discuss the main aspects that one should keep in mind when performing an incoherent

combination, and I will present the results of some tests that highlight the correct implementation of this part of the algorithm.
Finally, in Chapter 4, I will present the results of the application of these methods to the third LIGO-Virgo data-taking run searching for r-mode signals from PSR J0537-6910. I will briefly present the general characteristics of the O3 run, and then I will discuss the selected parameter space to perform this search, and the choice of the *inter-glitch* periods. Then, I will present the candidates of the search, even if it will not be possible to claim a detection. Finally, I will show how it is possible to set upper limits on the amplitude of an eventual r-mode CW, and the astronomical relevance of the obtained results. This last Chapter explores in detail the main results presented in the aforementioned LVK Collaboration paper [5].

Chapter 1

R-Mode Gravitational Waves

In this chapter, I will introduce the concept of r-mode oscillations of the fluid composing a pulsar and to discuss how these oscillations are related to Gravitational Waves (GWs) emissions. In particular, in Section 1.1, I will briefly sum up the description of r-modes obtained in [6, 7, 8, 9]. For the sake of clarity, in Sec. 1.2, I will present a brief discussion on Continuous Gravitational Waves (CWs) in general, using the main results from [10].Then, in Section 1.3, I will provide an overview about the coupling between r-mode excitation and GWs emission, as presented in [11]. Moreover, in Section 1.4, I will discuss the indications suggested by [12] to perform a search for r-mode gravitational signals. These considerations have provided useful guidelines for the development of this project. Finally, in Section 1.5, I will outline the timing model of PSR J0537-6910 obtained by *NICER* telescope [13]. These provided us the measures of the pulsar rotational parameters and the *glitches* occurrences, which are crucial for performing this search.

1.1 What is an *R*-Mode?

The r-mode, also known as *Rossby wave*, is a toroidal mode of fluid oscillation for which the restoring force is the Coriolis force, as explained in [14]. Therefore, in the astrophysical framework, it only exists in a rotating star. In the last years, this kind of oscillations aroused a lot of interest in the field of GWs (see, for example, [4, 15]) since they are generically unstable to gravitational emission. For this reason, it is possible that the signal grows to large amplitudes, becoming a detectable source of CWs (as outlined in [16, 17]). In the next paragraphs, I will describe the most important characteristics of r-mode excitations and the related GWs emission.

1.1.1 Velocity Pattern due to *R*-Mode

The best way to understand the nature of r-mode oscillations, is to study their multipole structure and the velocity field that the fluid elements on the surface of the pulsar experience. In this paragraph, I will present a brief discussion on the r-mode speed pattern in the framework of Newtonian gravity, and to first order in the rotational frequency ν of the star (for a detailed discussion also including relativistic effects see [7, 18]). In this case, the r-mode is purely toroidal and the

Eulerian velocity perturbation $\delta\mathbf{v}$ depends on ν, on the stellar radius R and on the dimensionless amplitude of the mode α through the relation[19]:

$$\delta\mathbf{v} = \alpha \left(\frac{r}{R}\right)^{\ell} R\nu \mathbf{Y}^{B}_{\ell m} \mathrm{e}^{\imath\omega t}, \tag{1.1}$$

where $\mathbf{Y}^{B}_{\ell m} \equiv [\ell(\ell+1)]^{-\frac{1}{2}} r\nabla \times (r\nabla \mathrm{Y}_{\ell m})$ is the magnetic-type vector spherical harmonic ($\mathrm{Y}_{\ell m}$ being the standard spherical harmonics). A representation of the perturbation experienced by the fluid surface elements is reported in Figure 1.1. Moreover, it is interesting to discuss how the r-mode perturbation acts in different

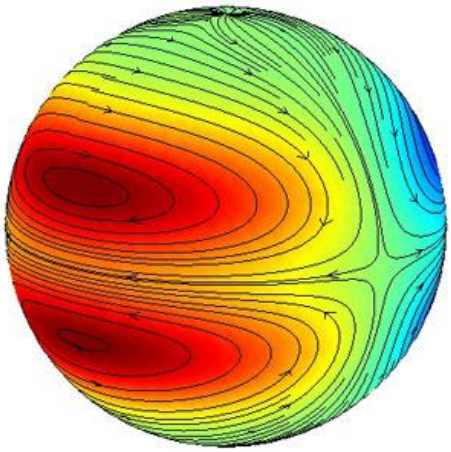

Figure 1.1. Pattern of velocity streamlines experienced by fluid elements due to r-mode oscillations. The restoring force for these perturbations is the Coriolis force. The gravitational emission coupled to these modes represent an interesting candidate for the detection of continuous gravitational waves. **Credit: N. Andersson.**

reference frames[1]. In particular, an important concept is the pattern speed, i.e. the field of the velocity perturbations on fluid elements. The following analysis is adapted from [7].
Since every mode has an expression of the form $\mathrm{e}^{\mathrm{i}(\omega t + m\phi)}$, where ω is the mode pulsation, ϕ is the phase and m is given by the order of the spherical harmonic, we can see that surfaces of constant phase are described by $m\phi + \omega t = \text{constant}$. Thus, one can compute the differential phase velocity $\sigma = \frac{d\phi}{dt} = -\frac{\omega}{m}$ in each point, in order to describe the pattern of the induced perturbation. The expressions one can find respectively for a rotating and for an inertial observer are:

$$\sigma_r = -\frac{2\nu}{\ell(\ell+1)}, \tag{1.2}$$

$$\sigma_i = \frac{(\ell+2)(\ell-1)}{\ell(\ell+1)}\nu. \tag{1.3}$$

[1]Some interesting animations describing the r-mode speed pattern can be retrieved at `http://research.physics.illinois.edu/CTA/movies/r-Mode/`

Thus, it is clear from the signs that, even if the r-mode appear retrograde in the rotating system, an inertial observer would view it as prograde. An additional representation of the r-mode velocity field is also given in Figure 1.2.

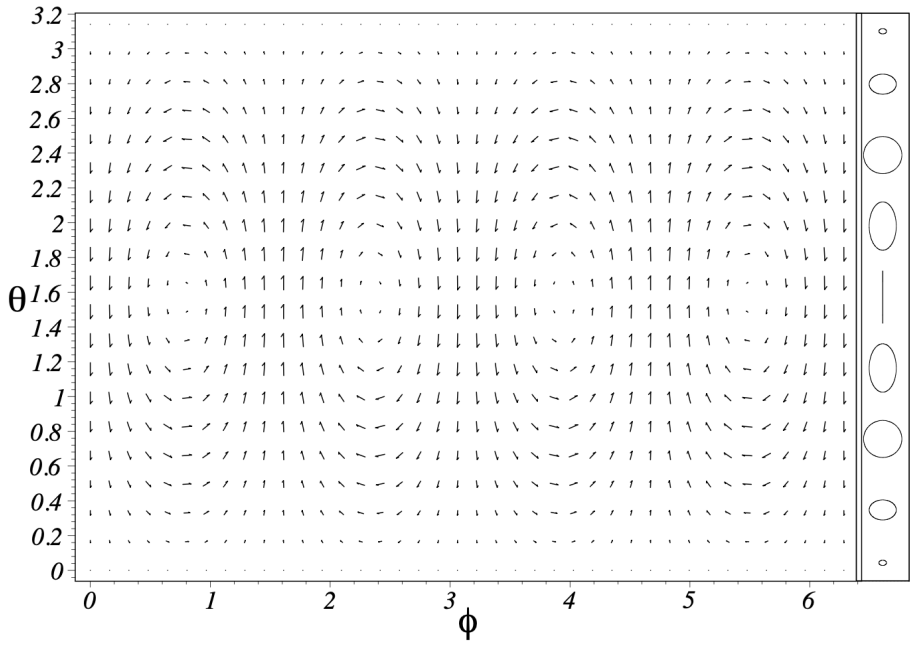

Figure 1.2. Velocity field of the r-mode as a function of the angular coordinates spanning the surface of the star. The narrow frame on the right is a qualitative depiction of the actual motion of individual fluid elements. **Credit: N. Andersson.**

1.2 Continuous Gravitational Waves

In general, GWs can be considered as small perturbations in a given space-time background. Thus, in the case of a flat background, it is possible to express the metric tensor $g_{\mu\nu}$ (which describes space-time curvature; $\mu, \nu = 0, 1, 2, 3$) as $g_{\mu\nu} = \eta_{\mu\nu} + h_{\mu\nu} + \mathcal{O}\left(|h|^2\right)$, where $\eta_{\mu\nu}$ is the flat space-time Minkowski tensor, $h \equiv \eta^{\mu\nu} h_{\mu\nu}$, and $|h| \ll 1$. In addition, it is well known that the gravitational strain tensor, choosing to operate in the *Transverse Traceless* (**TT**) gauge, has only two degrees of freedom: h_+ and $h_\times$. In particular, the tensor can be written as:

$$h_{\mu\nu}^{\mathbf{TT}} = \begin{pmatrix} 0 & 0 & 0 & 0 \\ 0 & 0 & 0 & 0 \\ 0 & 0 & h_+ & h_\times \\ 0 & 0 & h_\times & -h_+ \end{pmatrix}. \tag{1.4}$$

The explicit expressions of the two relevant components are given by:

$$h_+ = h_{jk} \left(p^j p^k - q^j q^k \right) /2, \tag{1.5}$$

$$h_\times = h_{jk} \left(p^j q^k + q^j p^k \right) /2, \tag{1.6}$$

where h_{ij} $(i,j = 1,2,3)$ are the spatial components of $h_{\mu\nu}$ and p^i and q^i are orthonormal vectors perpendicular to the wave propagation direction.
One of the most interesting cases of continuous gravitational waves emission is that of GWs from rotating compact stars, usually referrred to as *CWs due to ellipticity*, as treated in [10]. It is important to notice that r-mode emission are not due to ellipticity, but the study of this case is particularly simple and it offers a benchmark for comparisons and analogies. It is possible to show that a rotating star indeed emits gravitational waves only if it does not have an axial symmetry. The wave generated by this process is an almost-monochromatic signal, continuously emitted for years. Therefore, it is usually referred as *Continuous Gravitational Wave*. As I will show, the frequency of this wave is approximately constant and equal to twice the pulsar rotational frequency ν. The main contibution to this emission is due to an unbalance in the components of the *inertia tensor* I_{ij}, which is defined as:

$$I_{ij} \equiv \int_V \rho \left(r^2 \delta_{ij} - x_i x_j \right) d^3x, \tag{1.7}$$

where ρ is the star density (assumed to be uniform for this derivation), the coordinates $\{x_i\}$ $(i,j = 1,2,3)$ are Cartesian (the center of the star is at the origin), and $r^2 = x_1^2 + x_2^2 + x_3^2$. Gravitational Waves emissions are linked to the mass quadrupole tensor q_{ij}, which is defined as:

$$q_{ij}(t) \equiv \frac{1}{c^2} \int_V T^{00}(t, \mathbf{x}) x_i x_j \, d^3x, \tag{1.8}$$

where T^{00} is the 00 component of the mass-energy tensor of the system. It is possible to link Equations (1.7) and (1.8) with an easy relation:

$$q_{ij} = -I_{ij} + \delta_{ij} q_k^k. \tag{1.9}$$

Furthermore, a useful quantity for characterizing GWs is the reduced mass quadrupole Q_{ij},:

$$Q_{ij} \equiv q_{ij} - \frac{1}{3} \delta_{ij} q_k^k, \tag{1.10}$$

which is traceless. In the (**TT**) gauge, one gets:

$$Q_{ij}^{\mathbf{TT}} \equiv \mathcal{P}_{ijkl} Q_{kl} = \mathcal{P}_{ijkl} q_{kl}, \tag{1.11}$$

where $\mathcal{P}_{ijkl}$ is the projector to the (**TT**) gauge (the explicit expression is not relevant for our purposes). Using this expression, it is possible to compute the expression of the spatial (**TT**) gravitational strain tensor $h_{ij}^{\mathbf{TT}}$ to the first order, starting from the projection of the reduced mass quadrupole tensor in the (**TT**) gauge. Namely:

$$h_{ij}^{\mathbf{TT}}(t,r) = \frac{2G}{c^4 r} \frac{d^2}{dt^2} Q_{ij}^{\mathbf{TT}} \left(t - \frac{r}{c} \right), \tag{1.12}$$

being r the distance from the source. This formula represents the mass quadrupole approximation, and it is the leading term of the multipole expansion that describes the complete GWs emission (the complete expression can be found in [20]). In fact, the next to leading order of the expansion (1.12) is composed by the mass octupole and the current quadrupole terms. The interesting point is that r-mode emissions come out by the quadrupole current term of this expansion [21].

1.2.1 Continuous Signals

The key aspect of Eq.(1.12) is that it gives a method to compute the polarization amplitudes $h_{+/\times}(t)$ in terms of the physical quantities involved in the emission process. In particular one can describe how the asymmetry in the components of I_{ij} generates gravitational waves. As a simplistic model, we can characterize a homogeneous ellipsoid having semiaxes a,b,c in its corotating frame by its inertia tensor:

$$I_{ij} = \frac{M}{5}\begin{pmatrix} b^2+c^2 & 0 & 0 \\ 0 & c^2+a^2 & 0 \\ 0 & 0 & a^2+b^2 \end{pmatrix} \equiv \begin{pmatrix} I_1 & 0 & 0 \\ 0 & I_2 & 0 \\ 0 & 0 & I_3 \end{pmatrix}, \tag{1.13}$$

where I_i is the principal moment of inertia along the axis i. From this relation, it is possible to derive the reduced quadrupole tensor in the inertial frame:

$$Q_{ij}(t) = \frac{I_2 - I_1}{2}\begin{pmatrix} \cos 2\phi(t) & \sin 2\phi(t) & 0 \\ \sin 2\phi(t) & -\cos 2\phi(t) & 0 \\ 0 & 0 & 0 \end{pmatrix} + const, \tag{1.14}$$

where $\phi(t)$ is the rotation phase, and it is defined as

$$\frac{d\phi(t)}{dt} = 2\pi\nu(t), \tag{1.15}$$

being $\nu(t)$ the time evolution of the star spinning frequency. In the simple case of constant rotation velocity $\nu(t) = \nu$, we have $\phi(t) = 2\pi\nu t$. It automatically follows that, if the ellipsoid is axisymmetric ($a = b$), there is not GWs emission. On the other hand, if we have a triaxial ellipsoid ($a \neq b \neq c$), we can characterize it through the *oblateness* ϵ:

$$\epsilon \equiv \frac{a-b}{(a+b)/2}. \tag{1.16}$$

It is easy to demonstrate that:

$$\frac{I_2 - I_1}{I_3} = \epsilon + \mathcal{O}(\epsilon^3). \tag{1.17}$$

Thus, neglecting $\mathcal{O}(\epsilon^3)$, we can write:

$$Q_{ij}(t) = \frac{\epsilon I_3}{2}\begin{pmatrix} \cos 2\phi(t) & \sin 2\phi(t) & 0 \\ \sin 2\phi(t) & -\cos 2\phi(t) & 0 \\ 0 & 0 & 0 \end{pmatrix} + const. \tag{1.18}$$

At this point, by using the mass quadrupole approximation (1.12) in the (**TT**) gauge, we can obtain the signal expression in terms of the strain amplitude h_0:

$$h_{ij}^{\mathbf{TT}}(t,r) = h_0 \mathcal{P}_{ijkl} A_{kl}\left(t - \frac{r}{c}\right), \tag{1.19}$$

being

$$h_0 = \frac{4G\nu^2}{rc^4} I_3 \epsilon = \frac{16\pi^2 G}{rc^4 P^2} I_3 \epsilon, \tag{1.20}$$

where $P = 2\pi/\nu$ is the rotation period of the star, and

$$A_{kl}(t) = \begin{pmatrix} -\cos 2\phi(t) & -\sin 2\phi(t) & 0 \\ -\sin 2\phi(t) & \cos 2\phi(t) & 0 \\ 0 & 0 & 0 \end{pmatrix}. \tag{1.21}$$

The measured strain at the detector depends on the direction of the observer relative to the star rotation axis through the term $\mathcal{P}_{ijkl}A_{kl}$. This dependence can be made explicit with the introduction of the parameter ι, which is exactly the angle between the line of sight to the source and the star spinning axis, and it helps us to identify the two components h_+ and $h_\times$:

$$h_+ = h_0 \frac{1 + \cos^2 \iota}{2} \cos 2\phi(t), \tag{1.22}$$

$$h_\times = h_0 \cos \iota \sin 2\phi(t). \tag{1.23}$$

It it possible to show that the relation $h_0 = \sqrt{h_+^2 + h_\times^2}$ holds. Thus, we have found that an interesting characteristic of triaxial spinning stars is that they emit GWs at a frequency f equal to exactly twice the pulsar rotational frequency ν:

$$f = 2\nu = \frac{2}{P}. \tag{1.24}$$

Rapidly rotating neutron stars have periods of the order of a few milliseconds. Typical values of the other parameters are $T \approx 10^{45}$ g cm^2, $\epsilon \approx 10^{-6}$, and the distance from the Earth is of the order of a few kpc for galactic sources. Thus, it is useful to express the strain amplitude as:

$$h_0 = 4.2 \cdot 10^{-24} \left[\frac{1 \text{ ms}}{P}\right]^2 \left[\frac{1 \text{ kpc}}{r}\right] \left[\frac{I}{10^{45} \text{ g cm}^2}\right] \left[\frac{\epsilon}{10^{-6}}\right]. \tag{1.25}$$

It is important to notice that this expression gives a simple estimate of the amplitude, based on an extremely simplified model. Usually, neutron stars are not homogeneous, and their density radial profile $\rho(r)$ is not known.
Many interesting searches for CWs due to ellipticity were recently performed (see, for example, [22, 23, 22, 24]), but it was not possible to claim a detection yet. However, signals due to ellipticity and r-mode emission both represent promising candidates for future detections of CWs.

1.2.2 Spin-down Limit

Concerning the quantities appearing in the strain amplitude estimate (1.25), usually, the spinning period P and the distance r of many galactic sources can be measured by electromagnetic observations. In addition, the moment of inertia I can be estimated once an Equation of State is chosen among those proposed by different models. On the other hand, the *oblateness* ϵ is usually unknown. It is useful to exploit astrophysical observations to set an upper limit on this parameter: many pulsars are spun down (i.e. their spinning frequency ν decreases) over time due to braking mechanisms such as electromagnetic or GW emission. Thus, it is possible to provide an upper limit on ϵ by measuring the spin-down rate of these pulsars and assuming

that energy is dissipated is lost only through the GWs channel. To this purpose, one defines the gravitational wave luminosity L_{GW} as the gravitational energy emitted by a source per unit time:

$$L_{GW} \equiv \frac{dE_{GW}}{dt}. \tag{1.26}$$

The energy carried by gravitational waves can be obtained with the procedure described in [10]. Using the quadrupole approximation (1.12), it is possible to obtain:

$$L_{GW}(t) = \frac{G}{5c^5} \left\langle \dddot{Q}_{ij}\left(t - \frac{r}{c}\right) \dddot{Q}_{ij}\left(t - \frac{r}{c}\right) \right\rangle, \tag{1.27}$$

where the Brill-Hartle average $\langle \cdot \rangle$ indicates that this quantity is averaged over several wavelengths. It is possible to show that, in the case of a triaxial spinning ellipsoid, and in the adiabatic regime, Eq. (1.27) reduces to:

$$L_{GW} = \frac{32G}{5c^5} \epsilon^2 I_3^2 \omega^6, \tag{1.28}$$

where $\omega = 2\pi\nu$ is the angular velocity of the star. On the other hand, in the Newtonian limit, the rotational energy of the pulsar and its derivative are:

$$E_{\text{rot}} = \frac{1}{2} I_3 \omega^2, \qquad \dot{E}_{\text{rot}} = I_3 \omega \dot{\omega}. \tag{1.29}$$

Thus, we can obtain the spin-down limit for the *oblateness* ϵ_{sd} by imposing that the energy lost through GWs emission L_{GW} is equal to the variation in the rotational energy $-\dot{E}_{\text{rot}}$:

$$\frac{32G}{5c^5} I_3^2 (2\pi\nu)^6 \epsilon_{\text{sd}}^2 \equiv I_3 (2\pi)^2 \nu |\dot{\nu}|. \tag{1.30}$$

Consequently:

$$\epsilon_{\text{sd}} \equiv \left(\frac{5c^5 |\dot{\nu}|}{512\pi^4 G \nu^5 I_3} \right)^{\frac{1}{2}}. \tag{1.31}$$

Finally, it is useful to substitute this expression in Eq. (1.20), in order to obtain the spin-down limit on the strain amplitude:

$$h_{\text{sd}} = \frac{1}{r} \left(\frac{5GI_3|\dot{\nu}|}{2c^3\nu} \right)^{\frac{1}{2}} = 8.06{\cdot}10^{-19} \left[\frac{1\ \text{kpc}}{r} \right] \left[\frac{I}{10^{45}\ \text{g cm}^2} \right]^{\frac{1}{2}} \left[\frac{\dot{\nu}}{\text{Hz/s}} \right]^{\frac{1}{2}} \left[\frac{\text{Hz}}{\nu} \right]^{\frac{1}{2}}. \tag{1.32}$$

This estimate is helpful when performing CWs searches, as it gives insights on the expected amplitude for an eventual signal. Thus, in principle, it can be compared to the gravitational detectors sensitivity, in order to understand if a particular signal is expected to be detectable or not.

1.3 Coupling between *R*-Modes and GWs

The aim of this Section is to provide an overview of the mechanism that couples r-mode excitations and GWs emission. It is important to keep in mind that this discussion helps us to qualitatively understand how these GWs are generated, but it is carried out considering classical and simplified models for the pulsar. However, for

derivations concerning PSR J0537-6910, relativistic corrections cannot be neglected, as we will see in Section 1.4.
R-Modes are indeed an interesting source of gravitational waves, since relativistic hydrodynamics predicts their instability due to the Chandrasekhar-Friedman-Schutz criterion [25]. In fact, the amplitude time evolution is driven unstable due to the fact that r-modes are prograde in the inertial frame and retrograde in the co-rotating frame, as previously mentioned. Actually, this criterion is derived in a classical framework: the generalization of this characteristic to the relativistic case is provided in [17]. The instability is due to the possibility for the star to find lower energy and angular momentum configurations, in which the mode amplitude can grow [9].
In the slow-rotation approximation, the frequency f for an inertial observer of the continuous gravitational wave coupled to the r-mode excitation can be obtained, for an inertial observer, from Eq.(1.3). Even if these modes are generically unstable for each choice of ℓ and m , we are interested in investigating mainly the $\ell = m = 2$ current quadrupole mode, which is most strongly coupled to gravitational waves emission [7]. For the fundamental $\ell = m = 2$ mode, one gets (directly from Eq. (1.3)):

$$f = \frac{4}{3}\nu. \tag{1.33}$$

Thus, even using simplified models, we can appreciate a fundamental difference between this case and the case of ellipticity emission, where we had $f = 2\nu$ (see Eq.(1.24)).
However, it is important to mention that this relation is not accurate when dealing with PSR J0537-6910: since it is the fastest spinning ($\nu \approx 62$Hz) known young pulsar, the approximations used to obtain this result are not valid. In fact, including also relativistic corrections, it is possible to determine a range of possible frequencies to explore, as I will discuss in Section 1.4. In particular, the value $f = \frac{4}{3}\nu$ will result to be even outside the selected range, due to the relativistic modifications.

1.3.1 Strain Amplitude

For a comparison with the case of ellipticity CWs, it is useful to derive expression for the strain amplitude of r-modes GWs analogous to those in Sec. 1.2. As discussed in [26], using the multipole moment formulas from [20], it is possible to obtain the strain amplitude associated with r-modes dominant contribution ($\ell = m = 2$):

$$h_0 = \frac{1}{r}\sqrt{\frac{8\pi}{5}}\tilde{J}MR^3\alpha\omega^3, \tag{1.34}$$

where r is the source distance, M and R are the pulsar mass and radius respectively, ω is the spinning velocity, α is the adimensional amplitude from Eq. (1.1), and $\tilde{J}$ is the dimensionless canonical angular momentum of the r-mode. This equation allows us to convert h_0 in terms of α for a fiducial value of the quantity $\tilde{J}MR^3$.
With an analogous procedure to that used for ellipticity CWs, it is also possible to obtain the spin-down limit for the strain amplitude [11]:

$$h_{\mathrm{sd}} = \frac{1}{r}\sqrt{\frac{10G}{c^3}I_3\frac{\nu|\dot{\nu}|}{f^2}}. \tag{1.35}$$

Thus, once an upper limit on the strain amplitude is obtained, it is possible to convert it in terms of the r-mode amplitude α using Eq. (1.34). I will discuss the behavior of the spin-down limit strain amplitude h_{sd} more in detail in Sec. 4.7.

1.3.2 Polarization Exchange

An important characteristic of r-mode signals is the polarization exchange in the components h_+ and $h_\times$. In fact, CWs due to r-mode activity will have different polarization than CWs from ellipticity. The polarizations exchange come from the fact that the gravitational strain tensor of a signal generated by quadrupole-current dominated emissions (such as r-modes) can be obtained from that of the usual mass-quadrupole emissions (such as ellipticity signals) simply by exchanging the relevant components in the following way [11]:

$$(h_+, h_\times) \longrightarrow (h_\times, -h_+)\,. \tag{1.36}$$

As explained in detail in Section 2.4, this exchange does not affect the results obtained using a pipeline built for searches for CWs due to ellipticity. In fact, this peculiarity of quadrupole current emissions is not relevant when dealing with upper limits estimation, and the same methodologies used for standard searches can be extended without any problem. However, this exchange should be considered in the case of a detection, since it affects the estimation of the signal parameters, as discussed in Sec.2.3.3.

1.4 *R*-Mode Gravitational Emission Parameters

The aforementioned models describing gravitational signals generated by r-modes are not adequate to perform a search for a signal from PSR J0537-6910. In fact, they have been carried out in a classical framework, while it is fundamental to include relativistic corrections when dealing with a neutron star having a significant spinning velocity, as in this case.
The actual theoretical models describing r-mode GWs emission present significant uncertainties (at least with respect to CWs due to ellipticity) when it comes to define the parameters of the expected gravitational signal. All the considerations reported in this section are obtained from [12], which provided useful guidelines on the parameter space regions to explore for this search.
The ratio between the r-mode signal frequency f and the pulsar rotational frequency ν will be labeled as A, while second order contributions are accounted for through the parameter B. Thus, one obtains the following set of relations:

$$f = A\nu - B\left(\frac{\nu}{\nu_K}\right)^2 \nu + \mathcal{O}\left(\frac{\nu}{\nu_K}\right)^4, \tag{1.37}$$

$$\dot{f} = A\dot{\nu} - 3B\left(\frac{\nu}{\nu_K}\right)^2 \dot{\nu} + \mathcal{O}\left(\frac{\nu}{\nu_K}\right)^4, \tag{1.38}$$

$$\ddot{f} = A\ddot{\nu} - \left(3 + \frac{6}{n}\right) B\left(\frac{\nu}{\nu_K}\right)^2 \ddot{\nu} + \mathcal{O}\left(\frac{\nu}{\nu_K}\right)^4, \tag{1.39}$$

where ν_K is the Keplerian frequency of the pulsar, physically defined as the frequency at which the pulsar is teared apart by the centrifugal force (the exact value depends on the Equation of State), $n \equiv \nu\ddot{\nu}/\dot{\nu}^2$ is the pulsar *braking index* and dots indicate time derivatives. These relations enclose fully relativistic gravity corrections via the A parameter. They are likely to be accurate as long as no other physical mechanism plays a significant role in the r-mode oscillation, e.g., a resonance between the core and crust oscillation frequencies (see [27]). The signs have been chosen in order to have both A and B positive; in particular, the sign of the second term is due to the effects of gravitational redshift and dragging of inertial frames on the Coriolis force, as explained in [28]. Notice that Equations (1.38) and (1.39) are simply the time-derivatives of Eq.(1.37).

As explained in [29], it is possible to show that the $\mathcal{O}\left(\frac{\nu}{\nu_K}\right)^4$ remainder in the previous relations is negligible except when the star is spinning almost at its Kepler frequency ν_K. In the case of PSR J0537-6910, we can easily check that the value of ν (obtained from from [13]) is one order of magnitude smaller than the value assumed for ν_K, which will be discussed in the next section. It is thus safe to neglect these corrections for the rest of the search.

It is interesting to notice that, inverting the aforementioned relations, an observation of $(\nu, \dot{\nu}, \ddot{\nu})$ and an estimation of ν_K, A and B provide the ranges for $(f, \dot{f}, \ddot{f})$ to be searched in principle. This will be the main subject of Sections 1.4.1 and 4.3.

1.4.1 Theoretical Constraints

The parameters A and B are both dimensionless numbers of order unity that depend on the pulsar Equation of State, on its mass M and on its radius R, which are all unknown. A detailed study is reported in Section 3.B of [12], while here I will report only the most relevant conclusions, which are valid for different pulsars and Equations of State:

- It is possible to estimate a significantly plausible range for the parameter A using the general relativistic slow rotation approximation for different equations of state. In particular, from the considerations in [30], one gets $1.39 \leq A \leq 1.57$, depending almost entirely on the ratio M/R.
- The range of B is affected by bigger uncertainties, but its contribution is relevant only at second order. From the considerations reported in [12], it is safe to consider $0 \leq B \leq 0.195$.
- The fastest observed spinning frequency for a neutron star is about 716Hz, registered for PSR J1748-2446ad [31]. Since ν_K is expected to scale as $M^{\frac{1}{2}}$, to obtain more elastic limits (high B_{max}), one can assume that PSR J1748-2446ad is on the high end of the mass range and that the studied pulsar is on the low end. Usually, neutron stars having the same Equation of State have masses ranging over almost a factor of 2 [32]. Thus, it is safe to assume $\nu_K \simeq 716\text{Hz}/\sqrt{2} \simeq 506\text{Hz}$ [12].

It is important to notice that an eventual GW detection might provide insights on the pulsar structure: once f and $\dot{f}$ are known, A and B are automatically known.

These in turn can provide information on M and R and on the Equation of State [30, 29]. In this search, it was not possible to claim a detection, but the upper limits on the gravitational strain (reported in Section 4.6) also imposed some interesting astrophysical constraints, as discussed in Section 4.7.

1.5 PSR J0537-6910 *NICER* Timing Model

One of the peculiarities of PSR J0537-6910 is the relatively frequent occurrence of *glitches* i.e. sudden changes in the pulsar rotational frequency. An example of the rotational frequency ν time evolution when a *glitch* occurs is reported in Figure 1.3. Previous narrow-band searches for r-modes emission, such as [4], did not have the

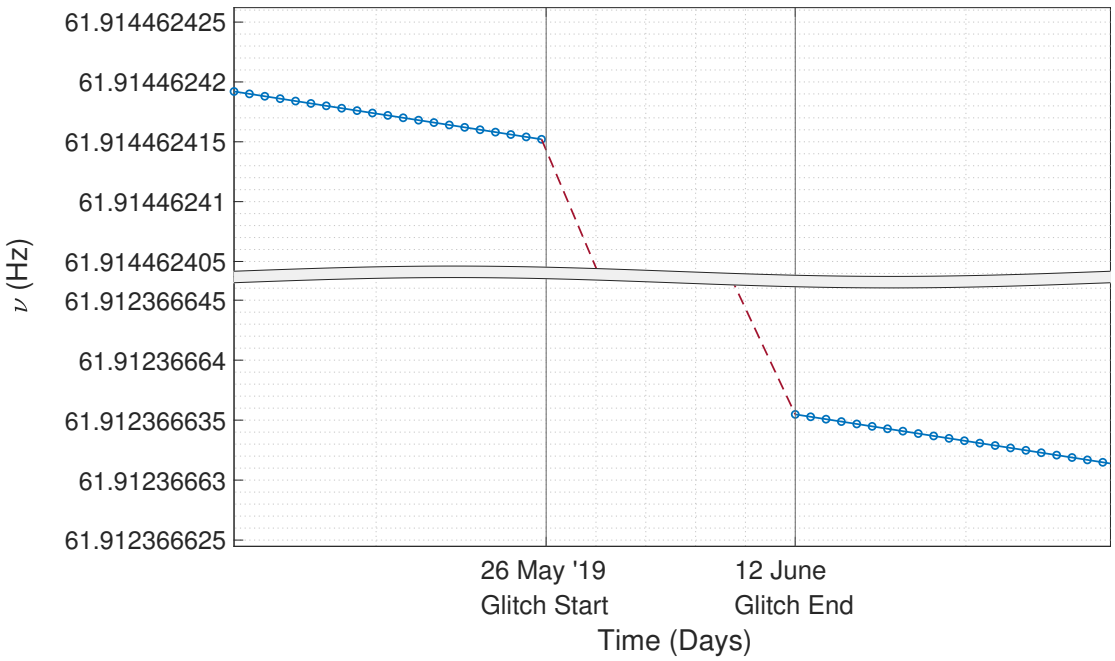

Figure 1.3. Time evolution of PSR J0537-6910 frequency around the first *glitch* occurred during the LIGO-Virgo O3 run. It is possible to see that the frequency decreases almost linearly (the effect of $\ddot{\nu}$ is negligible) in the *inter-glitch* periods (blue segments). In this regions, the phase evolution of the signal can be accurately modeled. Then, when the *glitch* occurs,there is a sudden change of frequency and spin-down (dashed red segment). In this period, there are complex mechanisms involving the pulsar fluid that do not allow for the phase evolution of the signal to be modeled.

possibility to account for the presence of *glitches*, since their occurrence was not timed. However, since the the gravitational signal frequency linearly depends on ν, it is evident that accounting for *glitches* brings important modifications to the expected signal model. For this reason, a search not accounting for the presence of glitches cannot be considered valid: it does not consider the changes in ν, which in turn yield modifications on the GW signal frequency. Thus, it becomes clear that

the timing model provided using the *NICER* telescope plays a key role in this search. The provided timing model identified three *glitches* during the LIGO-Virgo O3 run, which define four *inter-glitch* periods, as reported in Figure 1.4. For the actual search, the second period, which is the longest, will be split into two pieces, as better explained in Section 4.4.

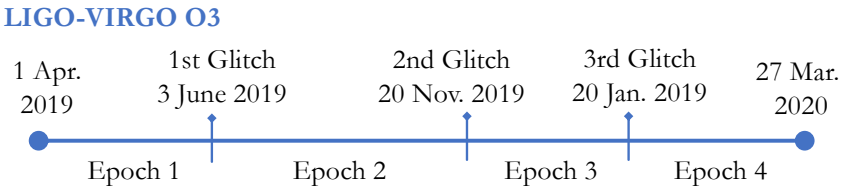

Figure 1.4. Occurence of *glitches* for PSR J0537-6910 during the LIGO-Virgo O3 run. Three *glitches* were detected during the searched time span.

1.5.1 Rotational Parameters

Combining different measurements, the *NICER* telescope team was able to perform a fit aiming at estimating the pulsar rotational parameters [13] . In particular, in Table 1.1, the rotational parameters of the pulsar are reported for the four *inter-glitch* periods overlapping the LIGO-Virgo O3 run. It was also possible to estimate the

Table 1.1. Rotational parameters of PSR J0537-6910 for the four time domain periods analyzed by the *NICER* telescope overlapping the LIGO-Virgo O3 run.

	MJD Start	MJD End	MJD Epoch	ν (Hz)	$\dot{\nu}$ (10^{-10} Hz/s)
1	58571.3	58629.3	58600	61.9145	-1.9974
2	58645.5	58804.5	58723	61.9124	-1.9973
3	58810.0	58862.9	58836	61.9104	-1.9974
4	58872.5	58964.4	58918	61.9090	-1.9977

parameters of the *glitches*, reported in Table 1.2. Notice that *glitches* last for many days (or at least their uncertainty covers a several-days time span): this aspect implies that some segments of data will have to be excluded from the analysis. It

Table 1.2. Parameters of the three *glitches* experienced by PSR J0537-6910 during the LIGO-Virgo O3 run measured by the *NICER* telecope.

	glitch Epoch (MJD)	$\Delta\nu$ (µHz)	$\Delta\dot{\nu}$ (10^{-13} Hz/s)
1	58637 ± 8	26.99 ± 0.01	-0.86 ± 0.04
2	58807 ± 3	7.57 ± 0.03	-2.2 ± 0.3
3	58868 ± 5	24.04 ± 0.08	-2.4 ± 0.5

is thought [33, 34] that *glitches* are activated due to the unpinning of superfluid vortices in the star's crust and possibly its core. Thus, it is not possible to model the phase evolution of the signal, in order to perform a coherent search when the *glitch* is happening. In fact, the strategy to carry out this search is to perform a

coherent search on *inter-glitch* periods, and then incoherently combine the results, as explained in 3.2.

1.5.2 The Importance of the *Braking Index*

The *braking index* is an important adimensional number that characterizes the spin-down behavior of a pulsar. It is defined in terms of the pulsar rotational frequency ν and its time derivatives as:

$$n = \frac{\nu\ddot{\nu}}{\dot{\nu}^2}. \tag{1.40}$$

The definition is directly linked to the typical power law followed by the spin-down rate $\dot{\nu} \propto -\nu^n$. The absolute value of the measured spin-down rate of PSR J0537-6910 increases over time. Performing a fit of all the measurements of $\dot{\nu}$ obtained joining data from the *NICER* and from the *RXTE* telescopes, it was possible to estimate the value of $\ddot{\nu}$ to be $\ddot{\nu} = (-8.00 \pm 0.08) \cdot 10^{-22}$ Hz/s^2. This measure directly provides a long-term *braking index* of $n = -1.25 \pm 0.01$ [13].
However, it is interesting to notice a peculiar characteristic of the behavior of the *braking index*: we can identify the *inter-glitch braking index* n_{ig}, which provides a measure of this quantity only on *inter-glitch* periods, thus neglecting the contributions brought by the presence of *glitches*. It can be observed that the long-term spin-down evolution of PSR J0537-6910 is strongly different from the behavior over short *inter-glitch* intervals. Between individual *glitches*, in fact, the *inter-glitch* braking index n_{ig} seems to asymptotically reach values of $n_{ig} \approx 7$ or possibly lower [13]. This observation confirms some previous results reported in [3, 35] . To explain this difference, it is thought that *glitches* could contribute to lowering the value of the braking index, as lower values of n are usually found for glitching pulsars [36, 37].

Emission Models

The main reason why it is important to study the behavior of the *braking index* of a pulsar is the fact that it provides insights on the mechanism that dissipate its rotational energy. In particular, it is interesting to consider the following cases:

- $n = 3$ is the canonical value for a pulsar whose rotational energy loss rate is purely due to electromagnetic dipole radiation [38] .
- $n = 5$ is obtained for GWs emission due to ellipticity. This would be the case of an emission as the one described in Sec. 1.2.
- $n = 7$ characterizes a spin-evolution dominated by r-mode activity [39]. This is the main reason why PSR J0537-6910 is an interesting candidate for this kind of GWs emission.

There are also other models that can produce a braking index below 3, such as a changing moment of inertia due to superfluidity [40] or time evolution of magnetic field orientation or strength [41, 42, 43, 44]. These models might be helpful to explain the behavior of the long-term *braking index*, but, since we are interested in GWs emission, we will focus on the value $n \approx 7$ for the short-term *braking index*.

From the previous considerations, it becomes evident that measuring an asymptotic value of $n_{ig} \approx 7$ suggests that constant amplitude r-modes could be activated in this pulsar, and the dissipated energy is emitted through this particular channel. Thus, the goal of this search is to identify possible signals due to this kind of emission.

Chapter 2

The Narrow-Band *5-Vectors* Pipeline

The main topic of this chapter will be the description of the narrow-band *5-vectors* pipeline. This algorithm has been developed over many years in the framework of the Rome Virgo CW group and it is particularly suitable to perform searches for CWs from well-localized pulsars with small uncertainties on their rotational parameters (of the order of 1Hz for the frequency and 10^{-10}Hz/s for the spin-down). Unfortunately, the narrow-band *5-vectors* pipeline cannot be applied to the case of PSR J0537-6910, given the fact that it is a fully coherent pipeline (it cannot account for *glitches*) and that the ranges of f and $\dot{f}$ needed for an r-mode search are above the pipeline capabilities (see Sec. 1.4). For this reason, I have extended the narrow-band pipeline to the case of glitching pulsars.
I will begin this Chapter by describing the main types of CW searches in Section 2.1. Moving on, in Section 2.2, I will provide some useful descriptions of the coupling between CWs and GWs detectors. In particular, I will introduce the narrow-band formalism, which is at the basis of this kind of searches.
Then, in Section 2.3 I will outline the main steps composing the narrow-band pipeline, used to perform coherent searches for r-mode signals only in the *inter-glitch* periods. The incoherent combination of the periods will be presented in Chapter 3.
Finally, in Sections 2.4 and 2.5, I will discuss the modifications needed to this pipeline in order to apply it to r-modes searches. Most of the material concerning the standard narrow-band *5-vectors* pipeline is taken from [45, 46, 47, 48].

2.1 Methods for Searching CWs

Algorithms used to perform CW searches aim at detecting the presence of a continuous signal embedded in noise. Usually, these algorithms carry out searches by comparing the data with a set of templates. which model the signal one expects to find in data. However, the key point is that one might know the waveform of the searched signal, but usually there is an uncertainty on the parameters shaping the waveform. The most relevant contributions are given by the rotational frequency ν of the pulsar, by its time derivatives $\dot{\nu}, \ddot{\nu}$ etc. , and by the target position in the sky, labeled by the two parameters α (right ascension) and δ (declination). The most common

procedure, is to discretize the parameter space introducing a grid in the parameters such that the signal-to-noise ratio loss due to the discretization is lower than a given threshold. As one expects, the wider is the parameter space that a search wants to explore, the larger will be the computation cost of the analysis. CWs searches are divided in three categories according to the degree of knowledge of the source:

1. **Targeted and narrow-band searches:** In this case, the parameters of the source are well measured and it is possible to perform a study based on matched filtering techniques in order to maximize the signal-to-noise ratio. The sensitivity h_{min} (i.e. the minimum detectable GW strain) of this type of searches scales with the observation time T_{obs} and detector noise spectrum S_f as:

$$h_{min} \approx \Theta \sqrt{\frac{S_f}{T_{obs}}},$$

   where the numeric coefficient $\Theta \approx 10$ for at a confidence level of 90% and to a false alarm probability of 1% (its exact value depends on the specific matched filter implementation). Therefore, it is important to have long data-taking time spans.

2. **Directed searches:** In this case, the position of the source is measured, but the rotational parameters are highly uncertain or unknown. This kind of searches is usually carried out by dividing the data in many different coherent data chunks, typically of the length $T_{coh} \approx days$, studying each chunk separately using matched filtering techniques, and then incoherently recombining the result of the different chunks. For these searches, the sensitivity is:

$$h_{min} \approx \frac{2}{3} \sqrt{S_f} \left(T_{coh} T_{obs}\right)^{-\frac{1}{4}},$$

   where T_{obs} is the detector observing time and S_f is the detector noise spectrum.

3. **All-sky searches:** This kind of searches does not assume a particular target and usually explores a large portion of the source parameter space. Usually semi-coherent procedures are used in order to identify the most significant candidates and study them with accurate follow-up procedures. In other words, data is divided into chunks, that are studied independently, in order to lately combine the results. The sensitivity for these kind of searches scales with the coherence time T_{coh} of each chunk, the number of data chunks N, and detector noise spectrum S_f as:

$$h_{min} \approx \frac{\Lambda}{N^{\frac{1}{4}}} \sqrt{\frac{S_f}{T_{coh}}},$$

   where Λ is a factor of order $\mathcal{O}(20)$ for $\mathcal{O}(10^9)$ selected candidates.

The computational resources needed for these searches usually scale with the magnitude of the studied time spans and of the parameter space.

R-Modes Searches

The goal of this kind of searches is to study the data in order to detect eventual signals, embedded in the interferometers noise, generated by r-mode activity. This thesis focus on the r-mode search using data produced by the LIGO-Virgo O3 run and the target is PSR J0537-6910. Targeted searches for continuous gravitational waves (CWs) are usually performed using coherent matched filtering techniques, which are particularly sensitive, but require the knowledge of the exact signal embedded in data. Unfortunately, in the case for r-modes CWs, it is not possible to model the signal when *glitches* occur, due to the complex mechanisms stepping in in this phase. Thus, it is not possible to define the phase relation of the signal along the whole time span. For this reason, the idea is to split the search into two pieces:

1. **Coherent Procedure:** It is possible to perform independent coherent searches for CWs in different *inter-glitch* periods. This search has been carried out using the tried-and-tested Narrow-Band *5-Vectors* pipeline, already applied to multiple searches for CWs due to ellipticity.

2. **Incoherent Procedure:** Results obtained on different periods have been incoherently combined. The underlying idea used to perform the combination is that the change in the rotational frequency ν of the pulsar will result in a change in the gravitational frequency f in different *inter-glitch* periods. This procedure is the main topic of Chap. 3

2.2 CWs in the Detector Reference Frame

In order to describe the methods used for the detection of gravitational signals, it is useful to describe how CWs are projected on gravitational interferometers (IFOs) using the following formalism. In particular, the detector responds to an incoming CW with the same principle of Michelson's interferometer, i.e., the wave induces a relative length change of the two IFO arms, which results in a measurable difference in the optical path of light traveling along the two arms. The detector response can be expressed as:

$$h(t) = \frac{1}{2}\left(\hat{n}_1\tilde{h}(t)\hat{n}_1 - \hat{n}_2\tilde{h}(t)\hat{n}_2\right), \tag{2.1}$$

where $\hat{n}_1$ and $\hat{n}_2$ are the unit vectors parallel to the two IFO arms and $\tilde{h}(t)$ is a 3-dimensional matrix describing the spatial components of the gravitational signal in the detector reference frame. $\tilde{h}(t)$ can be obtained by the spatial components of the gravitational strain in the **TT** gauge $h_{ij}^{\mathbf{TT}}$ (defined by Eq.(1.4), $i, j = 1, 2, 3$) applying a time-dependent rotation matrix $R(t)$:

$$\tilde{h}(t) = R(t)h_{ij}^{\mathbf{TT}}(t)R^T(t). \tag{2.2}$$

The rotation matrix $R(t)$ is given by the composition of three consecutive rotations. I will not give the explicit form of the three rotation matrices, but it is interesting to understand the steps from a physical point of view:

1. Rotation from the wave frame to the celestial sphere frame. This rotation depends on the GW polarization angle ψ (angle between the major semiaxis of the polarization ellipse and the celestial parallel of the source measured counter-clockwise) and on the source astronomical coordinates, i.e. the source declination (DEC.) δ and right ascension (R.A.) α.

2. Rotation from the celestial sphere frame to the Earth cardinal coordinates frame. The matrix describing this rotation will be time-dependent (due to the Earth motion) and it will be a function of the Earth sidereal frequency F_{sid}, on the detector latitude, and on a deterministic phase.

3. Rotation from the Earth cardinal coordinates frame to the detector reference frame. This rotation will depend on the interferometers location, on its orientation (a parameter γ labels the angle between the bisector of the arms and the East direction measured counter-clockwise), on the angle ζ between the two arms., and on the polarization angle ψ.

Combining these rotations, one can express, in a compact form, the detector response (i.e. the gravitational strain in the detector reference frame) as [45] :

$$h(t) = h_+(t)F^+(t,\psi;\alpha,\delta) + h_\times(t)F^\times(t,\psi;\alpha,\delta). \tag{2.3}$$

The functions $F^{+/\times}(t,\psi;\alpha,\delta)$ encode the detector response to each polarization, while the polarization amplitudes $h_{+/\times}(t)$ are the same encountered in Section 1.2, thus, they can be theoretically computed from the emission mechanism. Notice that these quantities are usually expressed in terms of the strain amplitude h_0 usign Eq.(1.22) and (1.23). The explicit expression of the functions $F^{+/\times}(t,\psi;\alpha,\delta)$ is:

$$F^+(t,\psi;\alpha,\delta) = \sin\zeta\left[a(t;\alpha,\delta)\cos 2\psi + b(t;\alpha,\delta)\sin 2\psi\right], \tag{2.4}$$

$$F^\times(t,\psi;\alpha,\delta) = \sin\zeta\left[b(t;\alpha,\delta)\cos 2\psi - a(t;\alpha,\delta)\sin 2\psi\right]. \tag{2.5}$$

By computing the coefficients $a(t;\alpha,\delta)$ and $b(t;\alpha,\delta)$ explicitly (see, for example, [6]), the interest of these expressions becomes evident. In fact, the contribution enclosed in these two functions is called *sidereal modulation*, since it depends only on harmonic contributions of five multiples of the Earth sidereal frequency: $f_i = k_i F_{sid}$, with $k_i \in [-2,-1,0,1,2]$. For this reason, we expect $h(t)$ to be a function of 5 frequency components: $[f-2F_{sid}, f-F_{sid}, f, f+F_{sid}, f+2F_{sid}]$, where f is the frequency of the gravitational signal. Thus, the power of the signal, which is generated by the pulsar as monochromatic, is split into 5 different components. This is the underlying idea which lead to the development of the *5-vectors* method for the detection of CWs.

The contributions from $h_{+/\times}(t)$ are called *fast harmonics*, since their phase evolution is faster than the one imprinted by Earth rotation and revolution. They depend on the GW polarization that arrive at the detector location without performing the projection on the IFO arms. The harmonic contribution of these terms depends entirely on f.

Moreover, there are relevant modulations due to some time-delay that occur during

the signal propagation in space that are not considered for in this derivation. The most important ones are the Rømer, the Einstein and the Shapiro delays. I will not discuss these modulations, but they are corrected when the analysis is performed, as explained in Section 2.3.

2.2.1 The Narrow-Band Formalism

To discuss narrow-band searches, the formalism firstly introduced in [46] is generally used. This formalism is completely equivalent to that of the previous section. However, while the latter one is helpful to understand how the physics is encoded in the detector response, the narrow-band formalism is handier to implement the actual search. The gravitational strain in the detector reference frame can be expressed as [49]:

$$h(t) = \mathrm{Re}\left[H_0\left(H_+ A^+(t) + H_\times A^\times(t)\right)\mathrm{e}^{\mathrm{i}\Phi(t)}\right]. \tag{2.6}$$

$\Phi(t)$ is the phase of the gravitational signal, and it is defined as:

$$\Phi(t) = \Phi_0 + 2\pi\int_{t_0}^{t} f(t')\,dt', \tag{2.7}$$

where $f(t)$ is the frequency of the signal as it is measured by the detector, and Φ_0 is the signal phase at the reference time t_0. We would expect the signal to be monochromatic, but the pulsar rotational frequency changes over time due to energy dissipation. The interest of this formula lies in the fact that all The functions $A^{+/\times}(t)$ encode the detector sidereal response, and they are defined as $A^+(t) = F^+(t, \psi = 0)$ and $A^\times(t) = F^\times(t, \psi = 0)$. $H_{+/\times}$ are complex polarization amplitudes, defined as:

$$H_+ = \frac{\cos 2\psi - \imath\eta \sin 2\psi}{\sqrt{1+\eta^2}} \qquad H_\times = \frac{\sin 2\psi + \imath\eta\cos 2\psi}{\sqrt{1+\eta^2}} \tag{2.8}$$

In these expressions, η is the ratio of the polarization ellipse semi-minor to semi-major axis, while ψ is the same polarization angle defined in 2.2. These amplitudes satisfy the normalization condition: $|H_+|^2 + |H_\times|^2 = 1$. The equivalence between the two formulations (2.3) and (2.6) is easy to prove once the following relations are provided:

$$\eta = -\frac{2\cos\iota}{1+\cos^2\iota}, \tag{2.9}$$

$$H_0 = \frac{h_0}{2}\sqrt{1 + 6\cos^2\iota + \cos^4\iota}, \tag{2.10}$$

ι being the angle between the line of sight and the star rotation axis, as in 1.2. This formalism is particularly useful to understand narrow-band searches since the *5-vectors* methods is based on the estimation of the complex amplitudes $H^{+/\times}$ from data, as I will show in Section 2.3.

2.3 The Narrow-Band *5-Vectors* Pipeline

In this section, I will describe the workflow of the narrow-band *5-vectors* algorithm, which is particularly suitable to study observed pulsars for which the position is well known, but the rotational parameters are not measured accurately enough to perform a matched filtering search based on a single point in the parameter space. In the case of PSR J0537-6910, the spinning frequency and its first time derivative are actually well measured by the *NICER* telescope, but the possibility to search wide ranges of frequencies an spin-downs is needed, since the r-mode emission model gives a wide range of possible frequencies and spin-downs, as seen in 1.4. Thus, this pipeline offers a powerful method to perform an r-mode search, even if some extensions will be needed, as I will discuss in 2.5.
The procedure for narrow-band searches has been firstly implemented in 2014 [47] and later extended [48]. Here, only a brief description of the most important steps is reported. A flow chart of the whole pipeline is reported in Figure 2.1. The

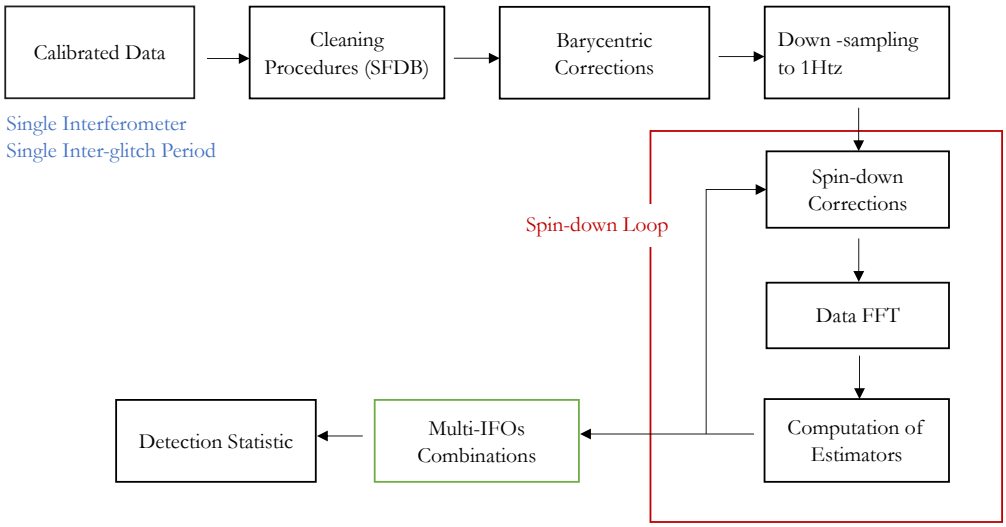

Figure 2.1. Flowchart of the narrow-band *5-vectors* pipeline.

calibrated data from the IFOs undergo a time-domain cleaning procedure in order to remove noise artifacts described in [50, 51] using algorithms involving Fast Fourier Transforms (FFT). The application of these procedures generates the Short FFT Database (SFDB), which is a collection of FFTs of several interlaced data chunks directly built from calibrated IFOs data [52]. Then, a frequency range containing the region one is interested in is extracted from the SFDB. At this point, the Doppler corrections due to Earth motion (see Section 2.2) are applied using the *stroboscopic resampling* technique, that I will describe in Section 2.3.1.
Moving on, one has to consider that the signal frequency decreases over time due because of the energy dissipation (due to EM and/or GW radiation) from the pulsar. This is the core part of the algorithm, and it consists in the application of the spin-down correction in a loop (one correction for each value of spin-down in a selected range) using the *heterodyne* technique, that I will treat in Section 2.3.2. For each

correction, the data FFT is computed, in order to compute the complex estimators $\hat{H}_{+/\times}$, as described in Section 2.3.3. This is the final result of a single-IFO coherent search. In fact, the corresponding estimators from different IFOs are combined as shown in Section 2.3.4, in order to produce the joint estimator. Finally, the detection statistic $\mathcal{S}$ is computed, as discussed in Section 2.3.5.
The obtained detection statistic will then be properly summed over the different *inter-glitch* periods. This will be the main topic discussed in Chapter 3 and it is the main extension needed in order to extend this pipeline to the study of r-mode signals.

2.3.1 Barycentric Corrections (*Stroboscopic Resampling*)

As discussed in Section 2.2, data has to be "translated" from the detector reference frame to the *Solar System Barycenter* (*SSB*) frame, which is (to a very good approximation) an inertial frame. Thus, the description of the wave in its frame, which is inertial (see Sec. 2.2) will be analogous to that in the *SSB*. This process is vastly simplified by the fact that the source position is well known for this kind of sources. The main contribution one has to consider is the Earth motion, which produces a Doppler shift (Rømer delay), but also Einstein and Shapiro delays have to be considered.

Rømer Delay: This contribution encloses the Doppler effect associated with the Earth rotation and revolution around the Sun. The frequency at the detector $f(t)$ can be expressed (in a non-relativistic framework) as a function of the emitted frequency $f_0(t)$:

$$f(t) = f_0(t)\left(1 + \frac{\vec{v(t)} \cdot \hat{n}}{c}\right), \tag{2.11}$$

where $\vec{v}(t)$ is the detector velocity with respect to the *SSB* $\hat{n}$ is a versor identifying the source position, and c is the speed of light. $\vec{v}$ is made of two contributions: the Earth revolution and rotation velocities. The inconvenient property of this correction is that it depends on the frequency itself. Thus, it affects every searched template in a different way. For this reason, for a monochromatic signal ($f_0(t) = f_0$), it is interesting to encode this correction in time domain, performing a resampling in the following way. Let us write the received signal phase $\Phi(t)$ as:

$$\Phi(t) = 2\pi \int_{t_0}^{t} f_0 \left(1 + \frac{\vec{v(t')} \cdot \hat{n}}{c}\right) dt' = \Phi_0 + 2\pi f_0 \left(1 + \frac{\vec{r(t)} \cdot \hat{n}}{c}\right), \tag{2.12}$$

where $\vec{r}(t)$ identifies the detector position with respect to the *SSB*, and Φ_0 is the initial phase of the signal. From Eq.(2.12), it is possible to see that now the signal phase has the same form of that of a monochromatic signal in terms of a new time variable τ:

$$\Phi(\tau) = \Phi_0 + 2\pi f_0 \tau, \tag{2.13}$$

$$\tau = t + \left(1 + \frac{\vec{r(t)} \cdot \hat{n}}{c}\right) \equiv t + \Delta_R(t). \tag{2.14}$$

The key advantage offered by this resampling is that now the correction does not depend on the frequency, thus, it is the same for all the templates of the search. The magnitude of this effect is $\mathcal{O}(10^3\text{s})$ per year.

Einstein Delay: This term has a relativistic nature: it accounts for the signal time delay due to Earth motion and the gravitational redshift at the Earth geocenter due to all the solar system bodies (except the Earth itself). It can be expressed as:

$$\Delta_E(t) \simeq \frac{1}{c^2} \int_{t_0}^{t} \left(U_\oplus + \frac{v_\oplus^2}{2}\right) dt', \tag{2.15}$$

where $U_\oplus$ is the gravitational potential at the geocenter due to all solar system bodies (except the Earth itself) and $v_\oplus$ is the velocity of the geocenter with respect to the *SSB*. This contribution cannot be computed analytically, thus only the first terms of the approximated expansion in [53] are effectively used.

Shapiro Delay: This terms accounts for the relativistic deflection of the signal traveling near massive bodies. For these purposes, the dominant contribution is given by the Sun. It can be expressed as:

$$\Delta_S(t) = -\frac{2GM_\odot}{c^3} \log(1 + \cos\theta(t)), \tag{2.16}$$

where $M_\odot$ is the mass of the Sun and $\theta(t)$ is the angle between the Sun-source direction and the Sun-detector direction. This effect is usually negligible for CWs sources, unless the source line of sight passes very close to the Sun.

From these considerations, it is clear that it is possible to account for these effects by performing a non-uniform resampling of the time variable. Therefore, a new time variable is introduced:

$$t' = t + \Delta_R(t) + \Delta_E(t) - \Delta_S(t), \tag{2.17}$$

where Δ_R, Δ_E, and Δ_S are the three delays defined above. The new time variable t' represents time in the *Solar System Baricentre*. An important aspect of this resampling is that it does not depend on the frequency, thus, it can be applied once and it holds for the whole search. At this point, data can be down-sampled to a sampling frequency not smaller than twice the width of the extracted band. Typically, a sampling frequency of 1Hz is used. The resulting time series is no longer affected by the barycentric modulation. This technique is called *stroboscopic resampling* and it is particularly suitable for this kind of searches since it does not depend on the signal frequency. Thus, it can be applied just once and holds for the whole search.

2.3.2 Spin-Down Corrections (*Heterodyne*)

As previously mentioned, one expects that the gravitational signal frequency $f(t)$ decreases over time, consistently with the decrease of the pulsar rotational frequency. This decline is due to the energy dissipation of the pulsar, which loses its rotational energy due to EM and/or GW emission. However, the diminishing of $f(t)$ is typically very slow: this justifies a Taylor expansion of the frequency around a fixed reference time t_0, which greatly simplifies the application of these corrections:

$$f(t) = f(t_0) + \sum_{k\geq 1} \frac{1}{k!} \left.\frac{d^k f}{dt^k}\right|_{t=t_0} (t - t_0)^k . \tag{2.18}$$

Usually, just the contributions for $k = 1, 2$ are relevant (this is true for the case of PSR J0537-6910), and these are also the ones reported in the pulsars ephemerides. Generally, uncertainties on the parameters are not relevant for CWs searches. At this point, one can integrate this expansion, in order to get the approximated spin-down phase evolution of the signal $\Phi_{sd}(t)$:

$$\Phi_{sd}(t) = 2\pi \int_{t_0}^{t} \sum_{k\geq 1} \frac{1}{k!} \left.\frac{d^k f}{dt'^k}\right|_{t'=t_0} (t' - t_0)^k \, dt' = 2\pi \sum_{k\geq 1} \frac{1}{(k+1)!} \left.\frac{d^k f}{dt'^k}\right|_{t'=t_0} (t' - t_0)^{k+1} . \tag{2.19}$$

Now, it is possible to compensate the decreasing of the signal frequency simply by multiplying data by the spin-down phase factor $\mathrm{e}^{-\mathrm{i}\Phi_{sd}(t)}$. In this way, there is an order-by-order cancellation of the terms. This result becomes evident substituting the expansion (2.18) in the phase definition given in Eq.(2.7). In fact, it is possible to write:

$$\Phi(t) = \Phi_0 + 2\pi f(t_0)\,(t - t_0) + \Phi_{sd}(t). \tag{2.20}$$

Therefore, using the expression from Eq.(2.6), one can directly obtain the corrected strain:

$$h'(t) = h(t)\mathrm{e}^{-\mathrm{i}\Phi_{sd}(t)} = H_0 \left(H_+ A^+(t) + H_\times A^\times(t)\right) \mathrm{e}^{2\pi \mathrm{i} f t + \mathrm{i}\phi_0}. \tag{2.21}$$

In this expression the frequency f is intended to be referred at the reference time t_0 (which should be always provided) and there is a redefinition of the overall phase $\phi_0 = \Phi_0 + 2\pi f t_0$. This particular technique that allows the frequency-changing signal to become monochromatic is called *heterodyne*.The interesting point of Eq.(2.21) is that now it can be seen as a fast monochromatic periodic term depending only on the frequency f modulated by a linear combination of harmonic terms of frequencies $\pm F_{sid}$ and $\pm 2F_{sid}$. Thus, coherently with 2.2, the signal can be completely described in terms of the 5 Fourier components of frequencies $[f, f \pm F_{sid}, f \pm 2F_{sid}]$.

Case of PSR J0537-6910. In the case of this particular search, it was possible to assume that the second derivative of the frequency is known (see Section 4.4) and that the higher order derivatives are null. Thus, one gets the following simple expressions:

$$f(t) = f(t_0) + \dot{f}(t_0)(t - t_0) + \frac{1}{2}\ddot{f}(t_0)(t - t_0)^2, \tag{2.22}$$

$$\Phi_{sd}(t) = 2\pi \left[\frac{1}{2}\dot{f}(t_0)\,(t - t_0)^2 + \frac{1}{6}\ddot{f}(t_0)\,(t - t_0)^3\right], \tag{2.23}$$

where the dot labels time derivatives. Thus, by substituting Eq.(2.22) inside Eq.(2.7) it is easy to show that Eq.(2.20) holds. It is also clear that the last step (Eq.(2.21)) works properly. This case is interesting because it helps us to understand how the spin-down corrections affect the computational load of the analysis. In this search, *inter-glitch* periods were selected in order that the second derivative of the frequency $\ddot{f}(t_0)$ can be considered fixed (see 4.4 for more details). Thus, the correction phase $\Phi_{sd}(t)$ only depends on one parameter: $\dot{f}(t_0)$. Thus, one initially selects an array of values of $\dot{f}(t_0)$, and the computational resources needed will scale linearly with the number of elements in this array. In fact, the spin-down cycle will iterate independently over each one of these values. On the other hand, if one should also select an array of values for $\ddot{f}(t_0)$, the needed resources would scale with the product of the numbers of elements of the two arrays. This aspect will lead to the choice (discussed in Section 4.4) of splitting an *inter-glitch* period into two pieces, in order for the assumption to keep $\ddot{f}(t_0)$ fixed.
Once the spin-down correction has been applied, the matched filtering procedure is used with templates spanning selected range of frequencies. From this procedure, it becomes evident why usually one refers to "grids" in the parameter space when performing this kind of searches: we have exactly built a bank of templates that can be labeled using a grid in the parameter space (f, $\dot{f}$).

2.3.3 Complex Estimators $\hat{H}_{+/\times}$ Evaluation

After the application of *stroboscopic resampling* and *heterodyne*, the signal embedded in data is monochromatic (apart from the sidereal modulation described in Sec. 2.3.1), and it has the form in Eq.(2.21), but the signal frequency is not known yet. For this reason, one has to compute the complex estimators $\hat{H}_{+/\times}$. These will be combined to get the detection statistic $\mathcal{S}$, which stores the information about the similarity between data and the template having the selected parameters.
To this purpose, the first important step is to compute a bank of data *5-vectors* $\vec{X}(f)$ (the arrow will label *5-vectors*), one for each spin-down correction. These are vectors composed by the five expected frequency components of the signal from 2.2, and they are built by computing the Discrete Fourier Transform (DFT) over the studied frequency region using the FFT algorithm. More details on this procedure can be found in [45, 48].
At this point, matched filtering is applied in the frequency domain. The matched filtering is computed using the *5-vectors* technique. Let us assume to have data $x(t)$ made of a monochromatic signal $h(t)$ of the form (2.21) embedded in noise $n(t)$: $x(t) = h(t) + n(t)$. Given a generic time series $g(t)$, the corresponding *5-vectors* is defined as:

$$\vec{G}(f) = \int_T g(t)\mathrm{e}^{-2\pi\mathrm{i}(f - \mathbf{k}F_{sid})t}\,dt, \tag{2.24}$$

where T is the total observation time and $\mathbf{k} = [0, \pm 1, \pm 2]$. To compute the matched filtering, it is necessary to build the *5-vectors* for data $x(t)$ and for the sidereal responses $A^{+/\times}(t)$. For data, one gets:

$$\vec{X}(f) = H_0 \mathrm{e}^{\mathrm{i}\phi_0} \left(H_+ \vec{A}^+(f) + H_\times \vec{A}^\times(f) \right) + \vec{N}(f). \tag{2.25}$$

Now, the matched filters are built by the complex scalar product between data and the normalized sidereal response *5-vectors*:

$$\hat{H}_{+/\times}(f) = \vec{X}(f) \cdot \frac{\vec{A}_{+/\times}(f)}{|\vec{A}_{+/\times}|^2}. \tag{2.26}$$

Thus, using this procedure, a couple of estimators will be computed for each frequency in the selected range. Considering that this set of operations is performed for each possible spin-down correction, it is evident that we will get a couple of estimators for each combination of parameters (f, $\dot{f}$, $\ddot{f}$, ...). These estimators will be used to build the detection statistic $\mathcal{S}$, as described in Section 2.3.5, in order to asses how much a signal with a given combination of parameters is compatible with data.

Parameter Space

When beginning a narrow-band search, one selects a range of frequencies Δf and its time derivatives $\Delta \dot{f}$, $\Delta \ddot{f}$, ... to explore. The search is then performed by discretizing these ranges according to a fixed step and study each point in the parameter space given by this discretization. The width of the frequency bin is $\delta f = \frac{1}{T}$, where T is the observation time of the search. The bin width for the i-th time derivative of the frequency $\delta f^{(i)}$ can be computed by imposing that an uncorrected amount of one bin produces a frequency variation over the total observation time T at most equal to half a frequency bin:

$$\frac{\delta f^{(i)} \cdot T^i}{i!} = \frac{\delta f}{2}. \tag{2.27}$$

Thus, for the first two orders, one gets:

$$\delta \dot{f} = \frac{1}{2T^2}, \qquad \delta \ddot{f} = \frac{1}{T^3}. \tag{2.28}$$

In this way, it is possible to obtain the number of studied points for each of these quantities:

$$n_f = [\Delta f \cdot T], \qquad n_{\dot{f}} = \left[\Delta \dot{f} \cdot 2T^2\right], \qquad n_{\ddot{f}} = \left[\Delta \ddot{f} \cdot T^3\right], \tag{2.29}$$

where $[\cdot]$ indicates the nearest integer. The total number of points in the parameter space will be given by the product of all these terms. In the case of the r-mode search from PSR J0537-6910, *inter-glitch* periods have been chosen in order to have $n_{\ddot{f}} = 1$, as discussed in 4.4.

Parameters Estimation

By substituting Eq.(2.25) in Eq.(2.26), it can be seen that the quantities $\hat{H}_{+/\times}$ are estimators respectively of the complex amplitudes $H_0 e^{i\phi_0} H_+$ and $H_0 e^{i\phi_0} H_\times$. For this reason if a detection is claimed, it is possible to provide estimators of the signal parameters using the following straightforward procedure. The signal amplitude will be obtained as:

$$\hat{H}_0 = \sqrt{|\hat{H}_+|^2 + |\hat{H}_\times|^2}. \tag{2.30}$$

On the other hand, it is possible to compute the quantities A, B, and C as:

$$\hat{H}_+ \cdot \hat{H}_\times = A + iB, \qquad |\hat{H}_+|^2 - |\hat{H}_\times|^2 = C, \tag{2.31}$$

where the dot labels the complex scalar product. Then, it is possible to estimate the parameter η as:

$$\hat{\eta} = \frac{-1 + \sqrt{1 - 4B^2}}{2B}. \tag{2.32}$$

Analogously, the polarization angle ψ estimation is given by:

$$\cos(4\hat{\psi}) = \frac{C}{\sqrt{4A^2 + B^2}}, \qquad \sin(4\hat{\psi}) = \frac{2A}{\sqrt{4A^2 + B^2}}. \tag{2.33}$$

2.3.4 Multi-IFOs Combination

The possibility to have data from a global network of detectors proves to be particularly helpful from different perspectives. For example, it might be useful in eventually triangulating the sky position of a GWs source, but it is also particularly interesting because it provides a better sensitivity. In fact, we do not expect noise artifacts to be correlated in different IFOs, while we expect in principle to measure a GWs signal on all of them.
Thus, the narrow-band *5-vectors* algorithm provides a method to coherently combine data from different detectors. This operation is specifically relevant for CWs searches, since eventual signals are particularly weak, but they are expected to be present in data for a long time span. The combination is coherent since it is performed right after matched filtering and it is performed consistently with the expected phase evolution of the signal. For this reason, it is important to consider the fact that data-taking periods usually do not begin exactly at the same time. Thus, it is important to use some precautions when performing the combination, for example, it is important to fix a common reference time. A more detailed discussion of these issues is provided in [45].
For the purposes of this thesis, it is useful to focus on the theoretical procedure used to combine data. As we have seen in Section 2.3.3, after performing the spin-down loop, the outcome will be a set of estimators $\hat{H}^i_{+/\times}$ for each detector (i is an index running over IFOs). It is possible to define the joint estimators $\hat{H}^J_{+/\times}$ as the weighted average of the single estimators, where the weights are the square modulus of the sidereal responses:

$$\hat{H}^J_{+/\times} = \frac{\sum_i \hat{H}^i_{+/\times} |\vec{A}^{+/\times}_i|^2}{|\vec{A}^{+/\times}_J|^2}, \tag{2.34}$$

where the joint modulus of the sidereal response $\vec{A}^{+/\times}_J$ is defined as the sum of the single responses:

$$|\vec{A}^{+/\times}_J|^2 = \sum_i |\vec{A}^{+/\times}_i|^2. \tag{2.35}$$

It is important to notice that the estimators are combined exactly with the same parameters (f, $\dot{f}$ etc.), i.e. , the grid built in the parameter space must be exactly the same in different IFOs, otherwise there might be a loss in the Signal to Noise Ratio (SNR). From the joint estimators and responses, it is possible to build the detection statistic.
In principle, another possible way to combine data is to build the single detection statistics of the interferometers and then to perform coincidences, i.e., to check if a possible candidate is measured in all the interferometers. However, it has been considered that the procedure of building the joint statistic is more useful to get an idea of what is measured overall by the detectors network. It is always possible to study what happens in single detectors as a follow-up procedure in the case a candidate is found.

2.3.5 Assessment of the Detection Statistic

After computing the estimators $\hat{H}_{+/\times}$ for all the possible combinations of (f, $\dot{f}$, $\ddot{f}$, ...), the aim is to quantify the agreement between data and the template having the give set of parameters. Thus, in standard narrow-band searches, the detection statistic $\mathcal{S}$ is defined as [47]:

$$\mathcal{S} = |\hat{H}_\times|^2 \cdot |A^+|^4 + |\hat{H}_+|^2 \cdot |A^\times|^4. \tag{2.36}$$

When performing a multi-IFO search, $\mathcal{S}$ is computed using the joint estimators $\hat{H}^J_{+/\times}$. However, the following considerations are independent on the number of interferometers used.
In the frequentist paradigm, it is possible to asses whether an obtained value $\mathcal{S}^*$ of the detection statistic is compatible with the hypothesis that a signal $h(t)$ is embedded in data $x(t)$. In particular, it is possible to estimate the corresponding p-value p^*, that is defined as the probability that $\mathcal{S}$ presents a value $\mathcal{S} \geq \mathcal{S}^*$ in the case of the null hypothesis, i.e., studying noise-only data:

$$p^* = P(\mathcal{S} \geq \mathcal{S}^* | h = 0). \tag{2.37}$$

One usually selects a threshold p-value p_{thr} (a typical choice in CW searches is $p_{thr} = 0.01$) and then performs a follow-up procedure on the candidates with a p-value smaller than the threshold. Interesting considerations on the nature of the candidates and how to carry out follow-up procedures is given in [45].
In order to compute the p-value, it is needed to estimate the noise probability distribution. It is possible to derive the analytic distribution under the assumption

that the noise is distributed as a Gaussian with mean zero and variance σ^2. In this case, it is possible to obtain the detection statistic probability density [47]:

$$f(\mathcal{S}) = \frac{\mathrm{e}^{-\frac{\mathcal{S}}{\sigma_X^2 |\mathbf{A}^\times|^2}} - \mathrm{e}^{-\frac{\mathcal{S}}{\sigma_X^2 |\mathbf{A}^+|^2}}}{\sigma_X^2 \left(|\mathbf{A}^\times|^2 - |\mathbf{A}^+|^2\right)}, \tag{2.38}$$

where $\sigma_X^2 = \sigma^2 \cdot T_{obs}$ is the variance of each component of the noise *5-vectors*, which is Gaussian as well, and T_{obs} is the observation time. Thus, the p-value for noise-only data is given by:

$$P(\mathcal{S} \geq \mathcal{S}^*) = \frac{|\mathbf{A}^\times|^2 \mathrm{e}^{-\frac{\mathcal{S}}{\sigma_X^2 |\mathbf{A}^\times|^2}} - |\mathbf{A}^+|^2 \mathrm{e}^{-\frac{\mathcal{S}}{\sigma_X^2 |\mathbf{A}^+|^2}}}{|\mathbf{A}^\times|^2 - |\mathbf{A}^+|^2}. \tag{2.39}$$

In practice, real noise cannot be model as Gaussian. For this reason, it is necessary to estimate the noise distribution using a different procedure, i.e., considering as noise a band of off-source frequencies close to the studied range. How this procedure has been applied to the case of PSR J0537-6910 will be described in Section 4.5.2. In addition, it is important to add that the detection statistic is usually normalized by a factor T^2, where T is the observation time. This normalization is needed when comparing $\mathcal{S}$ from periods having different duration, thus, it is fundamental in this search.

The *"Look-Elsewhere Effect"*

In this kind of searches, one usually explores a very large number of points in the parameter space looking for a signal ($N_{tot} \approx 10^9$ in the case of this r-mode search from PSR J0537-6910). For this reason, the probability that noise alone produces a high value of the detection statistic is increased. In fact, the aforementioned considerations are valid for estimating the single-trial noise probability density. Thus, we will need to impose a new significance threshold p_0 on the candidates, in order to take into account the *look-elsewhere effect*. The probability p_{above} that at least one of the computed values of $\mathcal{S}$ overcomes $\mathcal{S}_{p_0}$ is equal to 1 minus the probability that none of them is significant. Assuming that the searches are all independent, this probability is given by the product of the probabilities that each one of them is not significant. Thus, one finds:

$$p_{above} = 1 - (1 - p_0)^N. \tag{2.40}$$

It is possible then to impose $p_{above} = p_{thr}$ and to invert this relation in order to get the needed significance to have an interesting candidate p_0:

$$p_0 = 1 - (1 - p_{thr})^{\frac{1}{N}}. \tag{2.41}$$

This expression can be expanded for $p_{thr} \ll 1$ and large N:

$$p_0 \simeq \frac{p_{thr}}{N}. \tag{2.42}$$

Thus, potentially interesting candidates are those providing a p-value smaller than p_0. In the following chapters, I will also refer to the introduced factor $\frac{1}{N}$ in Eq.(2.42) as the multiplication by the *"trial factor"*.

Interbinning

In order to reduce the effect of spectral leakage due to frequency discretization, which can produce a sensitivity loss of up to $\sim 36\%$, we use an *interbinning* procedure [48]. This consists of estimating the data FFT values at the halfway bin $k + \frac{1}{2}$ in terms of the values at the k-th and $(k+1)$-th bins as

$$\tilde{x}_{FFT,k+\frac{1}{2}} \approx \frac{\pi}{4} \left(\tilde{x}_k - \tilde{x}_{k+1} \right). \tag{2.43}$$

The detection statistic is computed separately on the natural grid and on the grid of shifted bins, as I will discuss in Sec. 4.5.

2.4 Effects of the *R*-Modes Polarization Exchange

As derived in [11], and already mentioned in Section 1.3.2, the r-mode signal can be interpreted as a signal due to ellipticity where the polarization exchange in Eq.(1.36) is taken. For this reason, the strain components $h_+(t)$ and $h_\times(t)$ will be coupled to the detector responses as:

$$h(t) = h_\times(t) F^+(t,\psi) - h_+(t) F^\times(t,\psi). \tag{2.44}$$

Therefore, from Equations (2.4) and (2.5), it is possible to recover the standard narrow-band formalism simply by shifting the polarization angle ψ:

$$\psi \longrightarrow \psi + \frac{\pi}{4}. \tag{2.45}$$

Thus, using the expressions (2.8), it is evident that one can use the standard narrow-band formalism (which describes CWs due to ellipticity), as long as the following complex polarizations amplitudes exchange is intended:

$$(H_+, H_\times) \longrightarrow (H_\times, -H_+). \tag{2.46}$$

Therefore, the coupling between an r-mode signal and the detector can be expressed as:

$$h(t) = H_0 \left(H_\times A^+(t) - H_+ A^\times(t) \right) \mathrm{e}^{\mathrm{i}\Phi(t)}. \tag{2.47}$$

At this point, all the procedures described in 2.3 holds, and one can smoothly arrive to building the detection statistic $\mathcal{S}$ as it is defined in standard narrow-band searches. Thus, in principle it is possible to use a pipeline built for the detection of ellipticity CWs (such as the narrow-band *5-vectors* pipeline) also to estimate the detection statistic of r-mode signals, once the emission parameters are correctly specified.
The only case that requires caution is the parameters estimation of an eventual detection. It is true indeed that the detection statistic is well defined, but the complex estimators $\hat{H}_{+/\times}$ have a different meaning with respect to the case of CWs due to ellipticity. In fact, they are now estimators respectively of the complex amplitudes $H_0 \mathrm{e}^{\mathrm{i}\phi_0} H_\times$ and $-H_0 \mathrm{e}^{\mathrm{i}\phi_0} H_+$, which are different from the previous case. In this search, it was not needed to account for this discrepancy, since the detection statistic is not affected and it is the only relevant quantity when dealing with

upper limits estimation (see Section 4.6). However, in the case of a detection, one should estimate the source parameters ψ, and η using the procedure outlined in 2.3.3. These methods are not valid anymore, since one has to account for the aforementioned exchanges in the physical quantities, such as the amplitudes $H_{+/\times}$ and the polarization angle ψ.
Let's take an example to clarify this discussion: we can compute the estimator $\hat{H}_+$ from data as in Eq.(2.26). Since this is the result of the matched filtering performed using the sidereal response *5-vectors* $\vec{A}_+(f)$, it is correct that it is coupled to $\vec{A}_+(f)$ when building the detection statistic. For this reason, the standard definition of the detection statistic holds. On the other hand, it is important to consider that this estimator is not linked to the physical complex amplitude H_+, but it is an estimator of $H_0 e^{i\phi_0} H_\times$. Thus, this peculiarity has to be considered when recovering the physical parameters of the pulsar. For example, if one estimates the polarization angle using the procedure from 2.3.3, it should be considered that the computed $\hat{\psi}$ is related to the "fictious" ellipticity source. The estimator of the physical ψ_r of the r-mode source can be obtained as $\hat{\psi}_r = \hat{\psi} - \frac{\pi}{4}$.

2.5 Extentions Needed to Perform an *R*-Modes Search

As occasionally mentioned in the previous Sections, it is possible to perform the search for r-mode signals as a search for CWs due to ellipticity, but using some precautions. Three new main features are needed in order to perform an r-mode search:

1. ***Glitches*:** The main addition needed to perform an r-mode search is the introduction of a procedure to account for the presence of *glitches*. In fact, the time evolution of the gravitational signal has to account for the leaps occurring in the pulsar rotational frequency. Thus, it is possible to use the narrow-band *5-vectors* pipeline (which is fully coherent) only on separate *inter-glitch* periods. Then, the results can be incoherently combined. The description of how this combination is performed is the main topic of Chapter 3.

2. **Structured Parameter Space:** The standard narrow-band *5-vectors* pipeline is built to search over a rectangular region in the parameter space (f, $\dot{f}$), i.e., for each value of the spin-down corrections, the values spanned for the frequencies are the same. This aspect is not compatible with an r-modes search: as described in Section 4.3, the parameter space has the shape of a parallelogram. Thus, it is important to implement the extended pipeline in such a way that a different range of frequencies is selected for each value of the spin-down corrections.

3. **Different Source:** The original pipeline is built for CWs due to ellipticity, thus, it is already centered around the region of $f = 2\nu$. Of course this is not true in the case of r-modes: the gravitational frequency f mainly depends on the parameter A, which ranges between 1.39 and 1.57 (see Section 1.4). Thus, some modifications in this direction have to be implemented.

For these reasons, it was necessary to develop an extension of the standard narrow-band pipeline. This was my main contribution to this projects in terms of software development: I have implemented the modifications needed to account for these differences and the procedure to combine different *inter-glitch* periods, as I will describe in 3. Other relevant modifications are implemented in order to deal with a parameter space larger by a factor $\sim 10^4$ with respect to standard narrow-band searches. This is due to an enlargement factor of ~ 200 for the frequency and ~ 50 for spin-down rate. Thus, optimization schemes to manage the computational load have been developed. Then, I have applied the extended pipeline to the study of r-mode signals from PSR J0537-6910 during the LIGO-Virgo O3 run. I will present the obtained results in Chapter 4.

Chapter 3

Combination of *Inter-glitch* Periods

In this Chapter, I will describe how the combination of the results from different *inter-glitch* periods is performed. The underlying idea is that the change in gravitational frequency f of the signal between two different periods is only due to the corresponding leap in the rotational frequency ν of the pulsar.
I will begin with a general description of how an incoherent combination is performed and why it is needed in this case in Section 3.1. Then, in Section 3.2, I will describe the method used to perform the combination, which is based on using the physical parameters for providing an unique description of a given signal. In particular, in Section 3.3, I will treat the problem of finding the closest point on the grid given a set of parameters. In fact, for the feasibility of the search, it is fundamental that this operation is performed in an efficient way. Moving on, in Section 3.4, I will present an issue linked with the combination algorithm, which should be treated carefully. Finally, in Section 3.5, I will report the results of some tests highlighting the correct functioning of this algorithm.

3.1 Incoherent Combination

After the coherent part of the search, described in Chap. 2, a detection statistic $\mathcal{S}$ for each couple of frequency f and spin-down $\dot{f}$ has been computed. The second time derivative of the frequency $\ddot{f}$ has been fixed for the whole search, as described in Sec. 4.3. We know that different values of $\dot{f}$ correspond to the application of different spin-down corrections, while different frequencies have been studied by the matched filtering using *5-vectors* (see Eq.(2.26)). Thus, selected values for these two quantities comes from very different procedures, but they can be considered on the same level for the considerations outlined in this Section.
In fact, if is possible to think of the parameter space as a region in the plane $(f,\ \dot{f})$. This region is discretized according to the bins from Eq.(2.29), and there is a value of $\mathcal{S}$ corresponding to each one of these points. Moreover, it is important to keep in mind that, in the case of an r-mode search, the coherent procedure is applied independently on each *inter-glitch* period. The region searched in each period will be slightly different, since the change in ν affects also the ranges of f and $\dot{f}$ to analyze,

accordingly with Equations (1.37) and (1.38). As I will describe in Sec. 4.3, the region defined by the ranges on the physical parameters is shaped as a parallelogram. Finally, since the duration of the periods are not the same (see Sec. 4.4), the steps will be different too.
Since *glitches* are not accurately modeled, it is not possible to perform a coherent search during the whole O3 run (see 1.5). Thus, a clever procedure to overcome this difficulty is to incoherently combine the results from the independent coherent *inter-glitch* searches. This combination will be incoherent because it is not possible to account for the phase evolution of the signal: it will be performed directly at the level of the detection statistic.

3.2 The *Combination Algorithm*

The goal of the *Combination Algorithm* is to link the couples of parameters $(f,\ \dot{f})$ in different *inter-glitch* periods corresponding to the same physical signal. The basis for this combination procedure is offered by Equations (1.37) and (1.38). In fact, we expect that, when the *glitch* happens, the emitted signal will have a change in f and $\dot{f}$ associated with the changes in ν and $\dot{\nu}$:

$$\delta f = \left[A - 3B\left(\frac{\nu}{\nu_K}\right)^2\right]\delta\nu, \tag{3.1}$$

$$\delta \dot{f} = \left[A\dot{\nu} - 3B\left(\frac{\nu}{\nu_K}\right)^2\right]\delta\dot{\nu} - 6B\frac{\nu\dot{\nu}}{\nu_K^2}\delta\nu. \tag{3.2}$$

$\ddot{f}$ is expected to be the same along the whole search (see 4.3).In practice, The fundamental assumption we are making is that the coefficients A and B are constant in the two *inter-glitch* periods: since their value is related to the neutron star Equation of State, and thus should not be affected by *glitches*, this assumption is reasonable.
Given a couple $(f,\ \dot{f})$, it is possible to describe the signal using A and B by inverting Equations (1.37) and (1.38):

$$A = \frac{1}{2}\left(3\frac{f}{\nu} - \frac{\dot{f}}{\dot{\nu}}\right), \tag{3.3}$$

$$B = \frac{\nu_K^2}{2\nu^2}\left(\frac{f}{\nu} - \frac{\dot{f}}{\dot{\nu}}\right). \tag{3.4}$$

It is important to notice that this conversion depends on ν and $\dot{\nu}$, but we expect A and B to be always the same for the emitted signal. This is the key to the combination algorithm: f and $\dot{f}$ should change between different periods exactly in the way that keeps the values of A and B fixed.

3.2.1 Combination Implementation

After the coherent part of the search, one has a grid $(f,\ \dot{f})$ for each one of the *inter-glitch* periods. Each point of the grid is associated with a value of the detection

statistic $\mathcal{S}$. Thus, now it is necessary to link the points corresponding to the same physical signal in different grids. This coupling is performed in the following way:

1. **Computation of A and B:** Given a point i in the grid for the n-th *inter-glitch* period labeled by the gravitational parameters $(f_i^{(n)}, \dot{f}_i^{(n)})$, one can recover the value of A_i and B_i for the selected signal using Equations (3.3) and (3.4) with $\nu = \nu_n$ and $\dot{\nu} = \dot{\nu}_n$, where ν_n and $\dot{\nu}_n$ are the rotational parameters at the reference time for the period n (see Table 4.1). The important point is that A_i and B_i do not depend on n, since they are assumed to be constant, but only on the grid point label i.

2. **Parameters Evolution:** It is now possible to recover the *evolved* parameters $(f_{i_{ev}}^{(m)}, \dot{f}_{i_{ev}}^{(m)})$, where the *evolution* is performed using Equations (1.37) and (1.38) setting $A = A_i$, $B = B_i$, $\nu = \nu_m$, and $\dot{\nu} = \dot{\nu}_m$, where A_i and B_i are the parameters retrieved in the first step.

3. **Closest Point:** In general, the point $(f_{i_{ev}}^{(m)}, \dot{f}_{i_{ev}}^{(m)})$ does not belong to the grid of the m-th period. Thus, one selects the point j on the grid m having the parameters $(f_j^{(m)}, \dot{f}_j^{(m)})$ closest to $(f_{i_{ev}}^{(m)}, \dot{f}_{i_{ev}}^{(m)})$. The implementation of this step is discussed more in detail in Sec 3.3.

4. **Detection Statistic:** The normalized detection statistic of the points $(f_i^{(n)}, \dot{f}_i^{(n)})$ and $(f_j^{(m)}, \dot{f}_j^{(m)})$ is combined performing a weighted average. The weights are given by the inverse of the median of the power spectrum in the considered *inter-glitch* period.

A sketch outlining the incoherent combination procedure for two *inter-glitch* periods is reported in Figure 3.1. It is easy to see that this procedure can be easily generalized

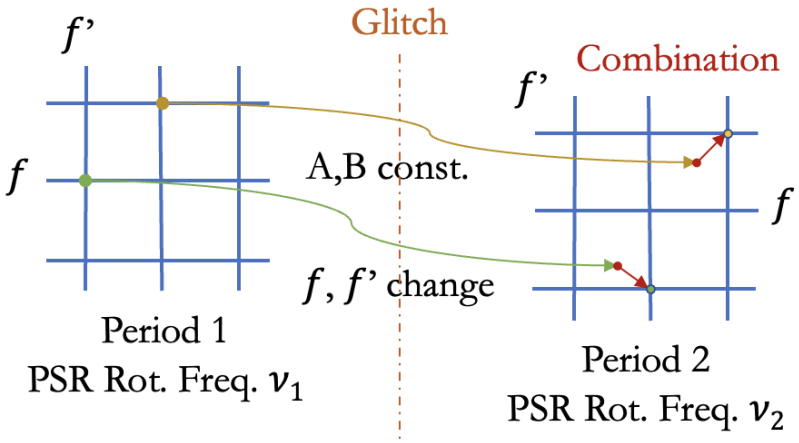

Figure 3.1. Sketch representing the combination of the detection statistic between different *inter-glitch* periods. The combination of the gravitational parameters in the different periods is performed assuming that the physical parameters A and B are constant. The change in f and $\dot{f}$ is due to the variation in ν and $\dot{\nu}$ after the *glitch*.

to all periods. In this way, it is possible to reconstruct the signal along the whole run.

It is important to notice that, in order to avoid the loss of studied grid points, the outlined combination procedure should be performed starting from the grid having the smallest steps (longest *inter-glitch* period, see Eq.(2.29)). In this way, multiple points from this grid will be associated to the same point in other grids.

3.3 Identification of the Closest Grid Point

The most computationally expensive part of the *combination algorithm* is represented by step 3 of the previously discussed implementation, namely the identification of the closest point on the grid. to the *evolved* parameters. In other words, suppose that we have taken a point in the first period and we have computed the *evolved* parameters in the second period. The *evolved* parameters will not belong to the grid in general, thus, the goal is to find the closest point that actually belongs to the grid. All the other operations can be easily *vectorized*, in order to be executed in an efficient way, while this one has to be computed singularly for each point.The aim will be to minimize the Euclidean distance between the *evolved* point and the grid points. It is possible to define indeed the following notion of distance between two points (f_1, $\dot{f}_1$) and (f_2, $\dot{f}_2$), measured in units of grid steps:

$$d_{1,2} = \sqrt{\left(\frac{f_1 - f_2}{\delta f}\right)^2 + \left(\frac{\dot{f}_1 - \dot{f}_2}{\delta \dot{f}}\right)^2}, \tag{3.5}$$

where δf and $\delta \dot{f}$ are the grid steps. This definition is necessary as the two quantities are dimensionally incompatible. Thus, reusing the notation from Sec. 3.2, the cleanest procedure would be to minimize $d_{j,i_{ev}}$ as a function of j, where j is an index spanning all the points of the grid and i_{ev} is the point labeled by the parameters ($f^{(m)}_{i_{ev}}$, $\dot{f}^{(m)}_{i_{ev}}$), which does not necessarily belong to the grid. In this way, one could find the point with the most similar parameters to those of the evolved point.
However, this procedure is computationally too expensive to be performed directly. Thus, it is necessary to find an alternative that allows a *vectorization* of the problem. The underlying idea one can exploit to perform the combination efficiently is that, before this steps, one already knows where the studied points are placed. In fact, the studied region will be a parallelogram (see Sec. 4.3) covering the grid in (f, $\dot{f}$). The situation will be similar to that represented in the sketch in Fig. 3.2. The important characteristic is the following: different lines correspond to the application of different spin-down corrections, but the studied frequencies are the same (if belonging to the parallelogram) for all the spin-down. This characteristic of the standard narrow-band pipeline comes from using an FFT algorithm, and it turns out to be particularly useful in this framework. In fact, due to this structure of the grid, it is possible to minimize the parameters one by one. In particular, in the practical implementation, the algorithm firstly finds which of the studied spin-downs $\dot{f}^{(m)}_j$,is the closest to the evolved one $\dot{f}^{(m)}_{i_{ev}}$. At this point, it is possible to retrieve the closest frequency to the evolved one $f^{(m)}_{i_{ev}}$ among the studied ones. However, one should notice that this procedure may fail at the edges of the selected region: this is the main topic of Sec. 3.4.
The difference between minimizing the function from Eq.(3.5) and minimizing the

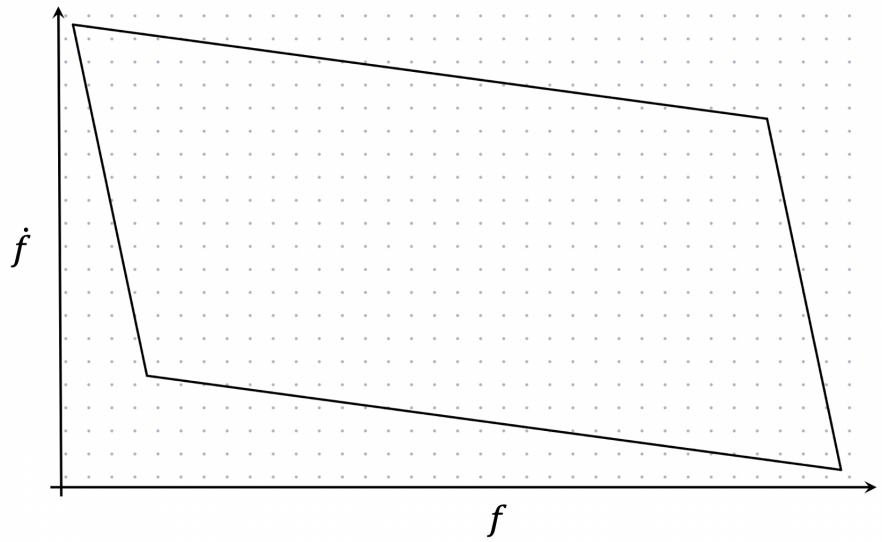

Figure 3.2. Sketch representing how the parameter space is structured. The selected region is a parallelogram overlapping the grid. The points represent grid points, and a value of the detection statistic is associated to each one of them. The important aspect is that the same values of frequency are studied for each value of the spin-down. This characteristic allows for an important speed-up in the combination procedure.

distance between the two variables separately is subtle, but it allows for a huge speed-up in the algorithm. In fact, one goes from minimizing a function of two variables to minimizing two functions of one variable. It is important to notice that this operation can be performed only due to the structure of the grid in the parameter space. In fact, if different values of frequencies were studied for each spin-down, it would not be possible to have this simplification.

3.4 Combination Problems

In this Section, I will deal with an issue related to the combination algorithm and having a parallelogram-shaped parameter space. In fact, as it will be explained in Sec. 4.3, Equations (3.3) and (3.4), given the thoretical ranges on the parameters A and B from Sec. 1.4, define a region in the parameter space $(f,\dot{f})$ shaped as a parallelogram. This aspect affects the combination algorithm, as it is possible to deduce by taking a look at Figure 3.3. As seen before, the combination mainly consists in the identification of the closest grid point to the parameters of the *evolved* point from the previous period. This identification is performed by firstly finding the closest spin-down, and then the closest frequency. It is possible to see that this technique does not work in the red-shaded regions in Fig. 3.3. In these cases, the closest spin-down leads to identifying a frequency outside the parameter space. At this point, there are two possibilities:

1. The closest point is the extremal value for the frequency range corresponding to the closest spin-down.

2. The closest point belongs to the next spin-down correction.

However, it is not possible to solve this problem *a priori*: when a frequency outside the range is obtained, it is necessary to compute the two distances (as in Eq.(3.5)) and to compare them. However, in this case, the distance of one of the two evolved parameters will differ by the evolved one by more than half grid step. For this reason, the search ranges have been enlarged, see 4.3, in order to ensure that these problems do not occur in the physical region,. This aspect has been also verified in the tests in 3.5

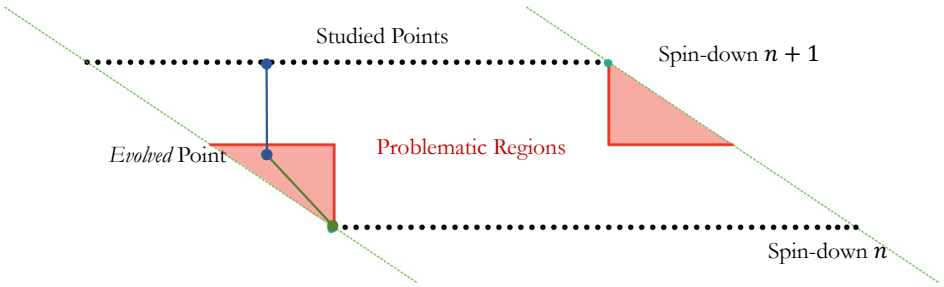

Figure 3.3. Sketch representing the issue concerning the combination of grids when the parameter space has the shape of a parallelogram. For the points in the red-shaded area, the combination algorithm does not work, since the obtained frequency would be out of the range. In this case, it is necessary to compute the distances in green and blue and then to see which of those is smaller. This procedure will identify the closest point to the *evolved* one.

3.5 Tests of combination

Multiple tests have been performed in order to verify the correct functioning of the algorithm. In this Section, I will present some tests concerning the distance between the *evolved* parameters ($f_{iev}^{(m)}$, $\dot{f}_{iev}^{(m)}$) and the closest point identified on the grid. I will present some results obtained on the complete parameters space and then the results on the physical regions, which are supposed not to be at the edges of the parallelogram.

3.5.1 Complete Space

Considering all the studied points, it is possible to study the mismatch between the evolved parameters ($f_{iev}^{(m)}$, $\dot{f}_{iev}^{(m)}$) from the previous Sections and the closest point on the grid. The results are reported in Figures 3.4 and 3.5. It is possible to see that,

in some cases, the mismatch is bigger than half bin: these cases are examples of the occurrences of the problem highlighted in Sec. 3.4. The reported tests have been performed on 1 dHz of the frequency range, corresponding to $\approx 1.9 \cdot 10^7$ points.

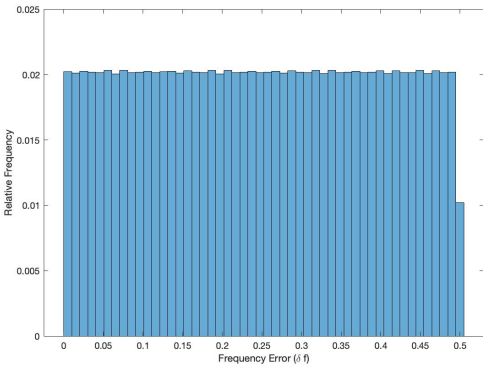

Figure 3.4. Frequency mismatch in units of δf. The effect of the problems at the edges can be seen for the values greater than half bin.

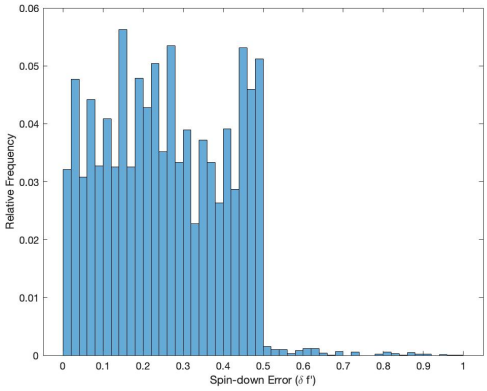

Figure 3.5. Spin-down mismatch in units of $\delta \dot{f}$. The effects of the problems at the edges can be seen for the values greater than half bin.

3.5.2 Physical Region

Results analogous to those previously presented, but limited only to the region where the parameters A and B belong to the physical ranges, are reported in Figures 3.6 and 3.7. In fact, the search is performed using enlarged parameters, and later excluding the regions at the edge. This procedure, is sufficient to solve the problem: in the physical region, the parameters are always closer than half bin.

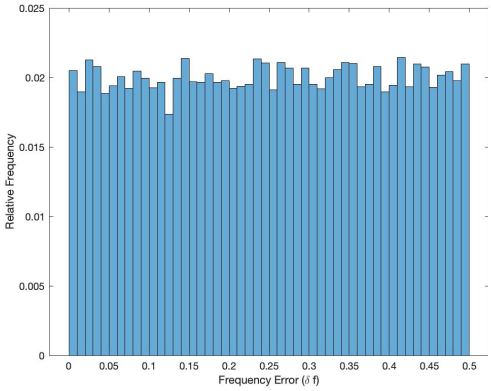

Figure 3.6. Frequency mismatch in units of δf. In the physical region there are no issues, since these regions are not at the edges.

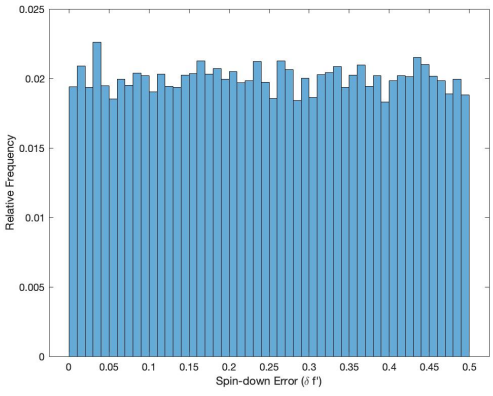

Figure 3.7. Spin-down mismatch in units of $\delta \dot{f}$. Also in this case, the problems at the edges are not present.

Chapter 4

The O3 Search

This Chapter follows the structure of the LIGO-Virgo-KAGRA Collaboration Paper [5], which reports the results obtained from this r-mode search from PSR J0537-6910. The main topic of the Chapter is indeed the application of the previously described methods to the LIGO-Virgo O3 run.
I will begin by describing the GW data from the interferometers (Sec. 4.1), and the ephemeris of PSR J0537-6910 (Sec. 4.2), which is fundamental to perform the search. Moving on, I will present an important discussion on the choice of the parameter space (Sec. 4.3) and the *inter-glitch* periods (Sec. 4.4). These topics have already been mentioned multiple times during the dissertation: here, an exhaustive treatment of these topics will be provided.
Then, in Section 4.5, I will present the results of the application of the extended pipeline to data and I will discuss how the significance of the candidates is evaluated. As none of the candidates is significant enough, the upper limits on the GW strain amplitude have been computed, and they are presented in Section 4.6. Finally, I will conclude this Chapter with the astronomical implications of the obtained results in Section 4.7.

4.1 The LIGO-Virgo O3 Run

Data used for this search have been taken from the third observing run (O3) of the two Advanced LIGO detectors [54]. Unfortunately, it was not convenient to use Virgo data to perform this search since the sensitivity[1] in the studied frequency region is significantly worse [55] . The O3 data-taking run lasted from 2019 April 1 to 2020 March 27, with a one-month pause in data collection in October 2019. The Hanford (H1) and the Livingston (L1) detectors had duty factors of $\sim 76\%$ and $\sim 77\%$, respectively during O3.
For this search, the studied data belong to the calibration having estimated amplitude and phase uncertainties of $\sim 7\%$ and $\sim 4\,\mathrm{deg}$ respectively [56]. These values are used as conservative estimates of the true calibration uncertainty near the frequencies region analyzed in this search.

[1] A useful characterization of the LIGO-Virgo detectors for the =3 run can be found at `https://dcc.ligo.org/LIGO-T2000012/public`

4.2 PSR J0537-6910 Ephemeris

In order to perform the search using the adapted narrow-band pipeline, it is fundamental to know exactly the position in the sky of PSR J0537-6910, in addition to the timing model provided by *NICER* and already presented in 1.5. This information is encoded via the two numbers α (right ascension) and δ (declination). The values are [57]:

$$\alpha = 05^{\mathrm{h}}37^{\mathrm{m}}47.^{\mathrm{s}}416, \qquad \delta = -69^{\circ}10'19.''88. \tag{4.1}$$

In addition to providing information on timing, electromagnetic observations also provide insight into the likely orientation of the spin axis of the pulsar. PSR J0537-6910 is indeed associated with the supernova remnant N157B in the Large Magellanic Cloud. Observations of the pulsar wind nebulae (PWN) torus of the remnant have enabled an accurate measurement of the orientation of the axis of symmetry of the torus [58]. In fact, it is likely that the symmetry axis of the torus coincides with the spin axis of the pulsar. This observation enables us to estimate the values of the two parameters ψ (polarization angle) and ι (inclination angle) of the GWs signal. We have:

$$\psi = (2.2864 \pm 0.0384)\mathrm{rad}. \tag{4.2}$$

For what concerns ι, we cannot obtain the absolute direction of the rotation of the pulsar from EM observations: we have two possible values of the inclination angle ι or $\pi - \iota$ [59]. Thus the measurements yield:

$$\iota = (1.522 \pm 0.016)\mathrm{rad}, \qquad \iota = (1.620 \pm 0.016)\mathrm{rad}. \tag{4.3}$$

This information can be used to carry out a version of the search where this prior information on these two angles is incorporated into the search, as will be described in 4.6. Unfortunately, an inclination angle ι close to $\pi/2$ means that the GW signal is almost linearly polarized and consequently it has nearly the smallest maximum signal-to-noise ratio achievable. In fact, it affects the strain amplitude, thus, the obtained upper limits for the signal amplitude.

4.3 Parameter Space

The goal of this Section is to properly define the parameter space used for this search, i.e., the points one has to investigate in the plane f-$\dot{f}$. The second derivative of the frequency can be considered fixed, as I will discuss in the following paragraph. Thus, only one point in $\ddot{f}$ is explored.
The region to investigate in the parameter space of f and $\dot{f}$ is defined by substituting the relations for A and B (Equations (3.3) and (3.4)) in terms of f and $\dot{f}$ into the constraints $1.39 \leq A \leq 1.57$ and $0 \leq B \leq 0.195$, namely:

$$1.39 \leq \frac{1}{2}\left(3\frac{f}{\nu} - \frac{\dot{f}}{\dot{\nu}}\right) \leq 1.57, \tag{4.4}$$

$$0 \leq \frac{\nu_K^2}{2\nu^2}\left(\frac{f}{\nu} - \frac{\dot{f}}{\dot{\nu}}\right) \leq 0.195. \tag{4.5}$$

These equations produce a parallelogram shape in parameter space, as shown in Figure 4.1, and reduce the volume to be searched over by a factor of 31 with respect to the choice of a rectangular grid in $(f, \dot{f})$. For this reason, the pipeline was extended in order to account for a parallelogram-shaped parameter space. In

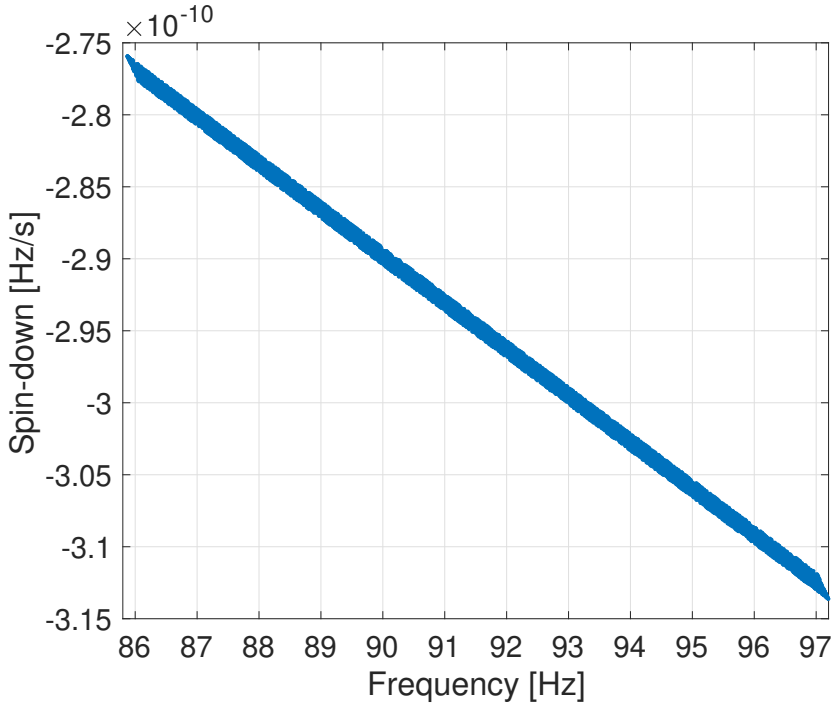

Figure 4.1. Representation of the explored region in the parameter space of f and $\dot{f}$. It is necessary to explore a wide range of frequencies due to the uncertainty on the parameter A, which represents the first-order ratio between the gravitational frequency f and the rotational frequency of the pulsar ν.

addition, to ensure computational accuracy, due to the issues at the edges outlined in Sec. 3.4, the search was initially performed slightly enlarging the physical ranges of the parameters (i.e., $1.38 \leq A \leq 1.58$ and $-0.01 \leq B \leq 0.205$).The central step of the *5-vectors* pipeline is the application of spin-down rate corrections, described in Sec. 2.3.2. Then, to cover this region in the parameter space a different frequency band is selected for each value of the spin-down rate. The correct frequency range for each spin-down rate is obtained by solving Eq.(1.38) for A and substituting it into Eq.(1.37) in order to get

$$f = \frac{\dot{f}}{\dot{\nu}}\nu + 2B\left(\frac{\nu^2}{\nu_K^2}\right)\nu. \tag{4.6}$$

From this relation, it is possible to obtain the values of the frequencies to study as a function of the spin-down rates by assuming $0 \leq B \leq 0.195$. The frequency step is $\delta f = 1/T$, while the spin-down is discretized in bins of width[2] $\delta \dot{f} = 1/T^2$. The selected region depends also on the value of ν, thus, we will have slightly different parallelograms for different *inter-glitch* periods.

Frequency Second Derivative. The second derivative $\ddot{f}$ can be considered as constant (within one frequency bin) for periods of length $T < T_{\max}$, with $T_{\max} = (2/\ddot{f}_{\max})^{1/3}$, where $\ddot{f}_{\max}$ is the maximum value allowed for the second derivative of the signal frequency:

$$\ddot{f}_{\max} = \ddot{\nu} \left[A_{\max} - B_{\min} \left(\frac{\nu^2}{\nu_K^2} \right) \right]. \tag{4.7}$$

We decided to fix $\ddot{\nu} = 1 \cdot 10^{-20}\text{Hz/s}^2$ for all segments, which is consistent with *NICER* measurements reported in [13]. Then, assuming a braking index ≈ 7, we can write $\ddot{\nu} = 7\dot{\nu}^2/\nu$ which gives $T_{\max} \approx 75$ days. These considerations lead to the choice of the data segments to be studied coherently and independently, as reported in Sec. 4.4. Therefore, the second derivative is fixed for all segments for the *5-vectors* pipeline to the value $\ddot{f} = \bar{A}\ddot{\nu} = 1.48 \cdot 10^{-20}\text{Hz/s}^2$, where $\bar{A}$ is the average value for the first-order parameter A (second-order corrections are neglected to fix this value). The second-order spin-down bin is $\delta \ddot{f} \simeq 2/T^3 = 1.30 \cdot 10^{-20}\text{Hz/s}^2$ and is large enough to include the uncertainty in $\ddot{f}$ due to the unknown exact values of parameters A and B and to the measurement of $\ddot{\nu}$.

4.4 *Inter-glitch* Periods

From the considerations in Sections 4.1 and 4.3, it results that, when defining *inter-glitch* periods, one has to take into account two aspects:

1. The occurrence of the commissioning break, which lasted for the month of October 2019.
2. The duration of the second *inter-glitch* period, which is higher than $T_{\max}$ defined in Sec. 4.3.

Therefore, it is not possible to use the *inter-glitch* periods as they are given by the *NICER* timing model. In particular, in order for the second derivative of the frequency to be fixed, it is necessary to split the second *NICER* period into two segments. For this reason, the segments 2 and 3 of the search actually correspond to the same *inter-glitch* period (same rotational parameters). The parameters for the five resulting periods for the search are reported in Table 4.1. Between the end of the commissioning break and the second *glitch* of PSR J0537-6910, there were only 16 days of available data, which were not considered for this search. The five periods can be represented on a timeline, as in Fig. 4.2

[2] Notice that this definition differs by a factor 2 from the definition given in Sec. 2.3.3. In fact, this is an arbitrary definition.

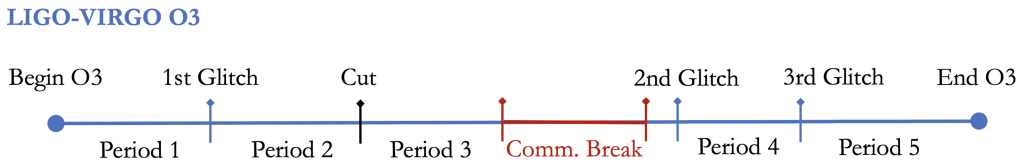

Figure 4.2. *Inter-glitch* periods considered for the r-mode search from PSR J0537-6910 during the LIGO-Virgo O3 run. Three *glitches* were detected during the searched time span. The second period was split into two segments in order for the assumption of $\ddot{f}$ being constant to be valid.

Table 4.1. Parameters of the five time domain periods analyzed. T is the duration of the period and N is the number of points in the parameter space. The chosen time periods are the same over which *NICER* provides the pulsar ephemeris.

Period	1	2	3	4	5
Start (MJD)	58574	58646	58701	58810	58873
Start Event	Start O3	1^{st} *glitch*	Cut	2^{nd} *glitch*	3^{rd} *glitch*
End (MJD)	58629	58701	58757	58863	58935
End Event	1^{st} *glitch*	Cut	Comm. Break	3^{rd} *glitch*	End O3
Epoch (MJD)	58600	58723	58723	58836	58918
T (MJD)	55	55	56	53	62
ν (Hz)	61.9145	61.9124	61.9124	61.9104	61.9090
$\dot{\nu}$ (10^{-10} Hz/s)	-1.9974	-1.9973	-1.9973	-1.9974	-1.9977
δf (10^{-7}Hz)	2.1898	2.1492	2.1492	2.3212	1.9026
$\delta \dot{f}$ (10^{-14}Hz)	4.7952	4.6191	4.6191	5.3880	3.6199
N	1.54×10^9	1.63×10^9	1.63×10^9	1.29×10^9	2.35×10^9

4.5 Search Candidates

Search candidates are obtained by selecting the loudest point (i.e. the point associated with the highest detection statistic) in each mHz of the studied frequency range. In fact, as mentioned in Section 2.3.5, two sets of candidates are selected: those with frequency in the natural grid and those with frequency belonging to the grid of shifted bins. The two sets of candidates are shown in the top and bottom panels of Figure 4.3, respectively.

It is clear from the figures that high values of the detection statistic correspond to several integer frequencies. They are due to disturbances of instrumental origin which mainly affect the Hanford detector[3]. Notice that, at this level, the parameters ranges are still enlarged of $\sim 10\%$($1.38 \leq A \leq 1.58$ and $-0.01 \leq B \leq 0.205$). For these reason, some vetoes are applied to the candidates.

[3]A list of known instrumental spectral disturbances can be found at https://www.gw-openscience.org/.

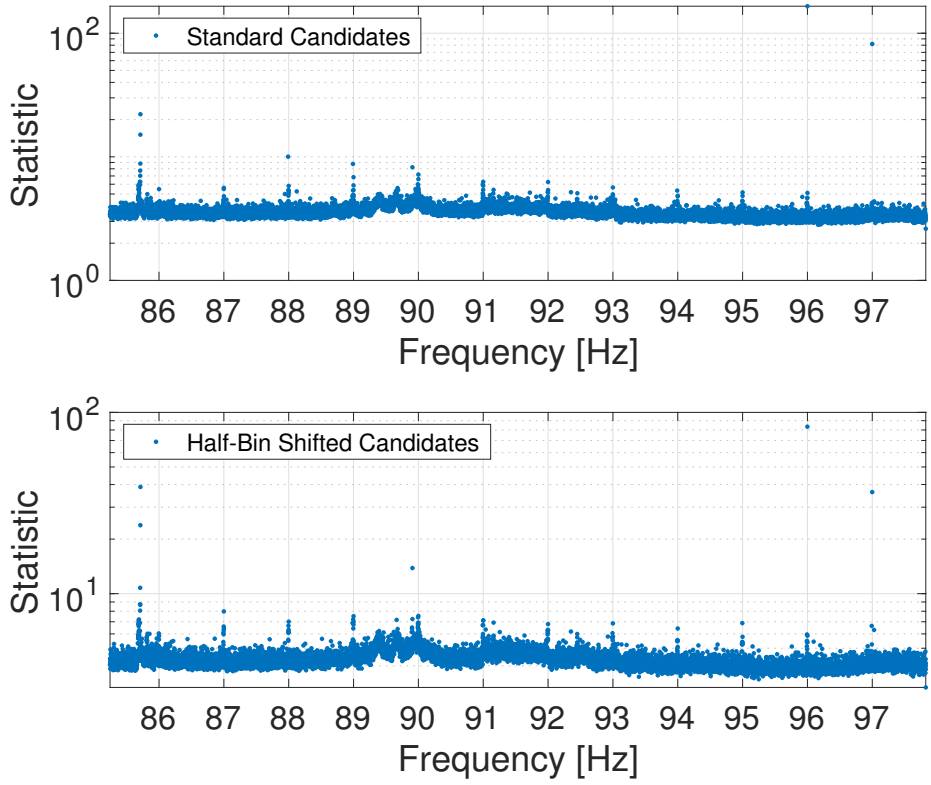

Figure 4.3. Normalized detection statistic for the full set of candidates on the natural and on the shifted search grid. Excess value of the detection statistic, due to detector disturbances, are evident at several integer frequencies.

4.5.1 Application of vetoes

To obtain more significant results, it is useful to exclude three sets of points from the candidates:

1. Candidates closer than 0.01Hz to integer frequencies. These points are removed in order to lower the impact of these disturbances on the estimation of the noise distribution, which is used to determine the significance of a given candidate, as explained in Sec. 2.3.5. In fact, if one considers these points, the noise is estimated as much higher than what it actually is in between integer frequencies, since it is affected by these artifacts. An eventual candidate having a frequency closer than 0.01Hz to an integer value would be excluded, but it could not be detected anyway due to the presence of these disturbances. Thus, the overall search is enhanced by this exclusion, as it becomes more sensitive in the considered regions.

2. Candidates outside the physical ranges $1.39 \leq A \leq 1.57$ and $0 \leq B \leq 0.195$. These points can be safely excluded since, as already discussed in Sec. 1.4, these constraints are already considering a wide range of possibilities. Eventual

candidates in these regions cannot thus have a physical origin connected with r-mode excitation from PSR J0537-6910.

3. Candidates whose detection statistic in one segment is greater than the sum of the statistics on all the other four segments. We expect indeed that, even if the r-mode is re-activated after each occurring *glitch*, it is very unlikely that the excitation mechanism changes to the point that the gravitational energy dissipated in a single period is higher than the total energy emitted in all the other periods. On the other hand, it is more plausible to have temporary noise disturbances that might occur for a limited period of time, thus affecting only one of the studied periods. For these reasons, this veto is helpful in limiting the effect of temporary noise disturbances.

The candidates surviving after imposing these selection criteria are shown in Figure 4.6 (and discussed in Sec. 4.5.3) for the natural frequency grid and for the shifted one.
It is interesting to mention that the application of the vetoes results in a change in the *trial factor* N. In fact, the parameter space had been chosen to satisfy the first two conditions long before the computation of the detection statistic: the requirement on the physical ranges of A and B had been imposed at the beginning of the search (see Sec. 1.4), while the exclusion of the regions around the integer frequencies had been decided by studying the power spectrum of the uncorrected data from the Hanford interferometer in the relevant frequency range, which is reported in Fig. 4.4. The peaks at integer frequencies are already present before the application of Doppler and spin-down corrections, and this strengthens the belief that they do not have an astrophysical origin.

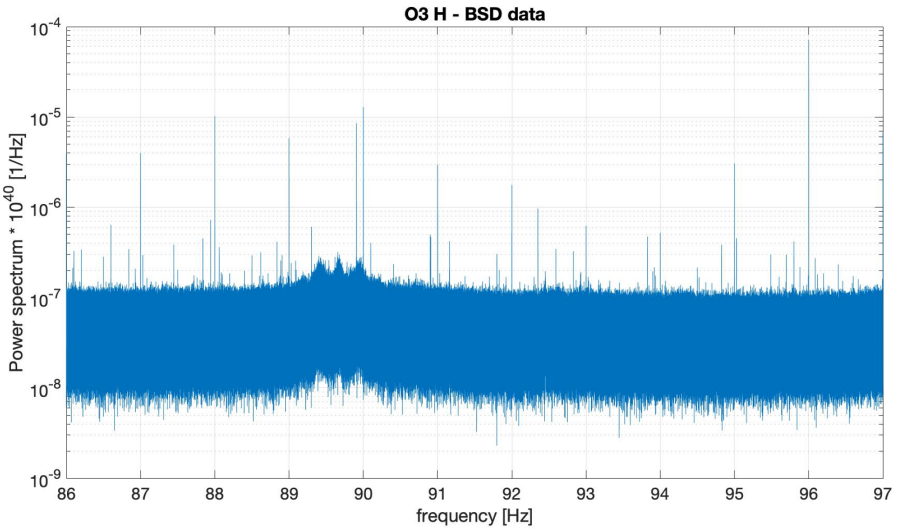

Figure 4.4. Power spectrum of the uncorrected data from the Hanford interferometer in the relevant frequency range. It is possible to see the disturbances at the integer frequencies, which completely alter the estimation of the noise distribution

4.5.2 Significance Assessment

For candidates surviving the imposition of vetoes, the significance is computed through the p-value, obtained by comparing the candidate detection statistic value to the distribution of the noise statistic. More specifically, the noise distribution is computed from the data itself, using the following procedure (adapted from [46, 48]):

1. As previously described, the loudest candidate is chosen for a given 1mHz band.
2. All the points in the 1Hz band which includes the candidate are selected (excluding the 1mHz band to which the candidate belongs). In addition, also all the points in the preceding and the following 1Hz bands are considered.
3. An histogram of the values of the detection statistic for all the points selected at the previous step is computed. This histogram represents an estimation of the noise distribution around the initially selected mHz.
4. The right tail (where loudest points are supposed to be) of the noise distribution is supposed to present an exponential behavior (as seen in Sec. 2.3.5). Thus, a linear fit of the tail in logarithmic scale is performed, in order to estimate the exponential decreasing rate of the distribution tail, as represented in Fig. 4.5.
5. The knowledge of the behavior of the tail of the noise distribution allows to simply estimate the p-value of the candidate. The explicit p-value estimation is discussed below.

Eventual candidates with p-value smaller than 1% (after properly taking into account the *trial factor*) undergo a follow-up procedure, aiming at increasing their significance or, conversely, at demonstrating that they are incompatible with an astrophysical GW signal.

***P*-Value Estimation.** After the histograms estimating the noise distribution is built, its right tail is linearly fitted in logarithmic scale, as it is expected to have an exponential decrease [47]. From the parameters of the fit, it is possible to evaluate the p-value for a given measured value $\mathcal{S}^*$ of the detection statistic. We expect the tail of the noise distribution $f(\mathcal{S})$ to behave as:

$$\log f(\mathcal{S}) \sim a\mathcal{S} + b. \tag{4.8}$$

The parameters a and b are exactly those estimated with a linear fit in logarithmic scale of $f(\mathcal{S})$ in the region of the tail, as shown in Figure 4.5. Notice that the parameter a will be negative. The p-value associated to a given value $\mathcal{S}^*$ is defined as the integral of the distribution from $\mathcal{S}^*$ to $+\infty$:

$$p(\mathcal{S}^*) = \int_{\mathcal{S}^*}^{+\infty} f(\mathcal{S})\, d\mathcal{S} \sim -\frac{1}{a} \mathrm{e}^{a\mathcal{S}^* + b}. \tag{4.9}$$

In this way, it is also possible to compute the values of $\mathcal{S}$ corresponding to a given significance: this is what has actually been done in the search. An overall p-value

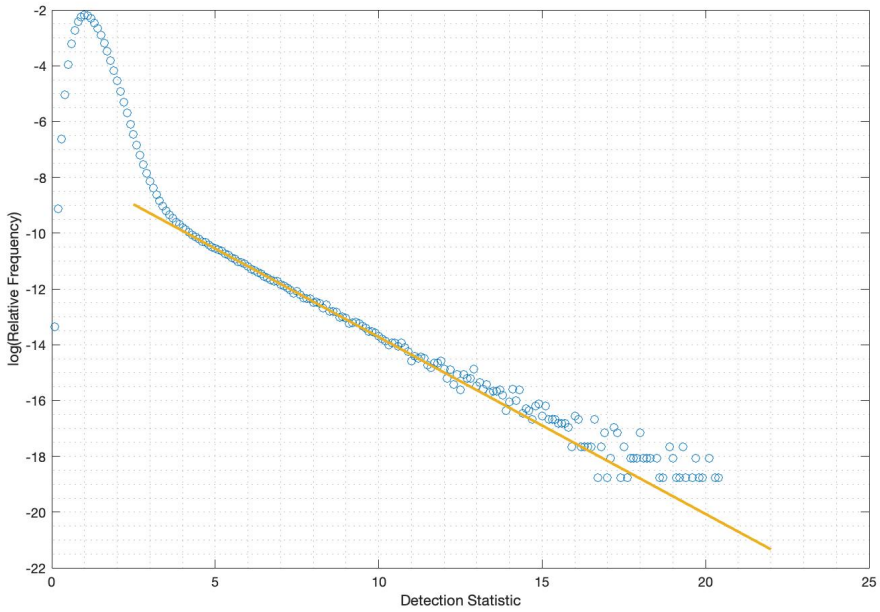

Figure 4.5. Example of the noise distribution histogram in the region $86 - 89$ Hz and of the linear fit of the tail, represented by the continuous yellow line. This fit enables us to estimate the decreasing rate of the tail, which allows to compute the p-value corresponding to a given value of the detection statistic.

threshold, p_{thr}, is computed such that $p_{\text{thr}} \cdot N_p = 0.01$, where N_p is the *trial factor* including the vetoes correction mentioned in Sec. 4.5.1. On this distribution the threshold on the detection statistic $\mathcal{S}_{\text{thr}}$ corresponding to p_{thr} has been computed and used to establish if that candidate is highly significant. $\mathcal{S}_{\text{thr}}$ plays an important role also in the computation of the strain amplitude upper limits, as shown in Sec. 4.6.1.

4.5.3 Final Search Candidates

As before, two sets of candidates surviving the vetoes procedures are plotted ion Fig 4.6: those selected in the natural frequency grid (top panel) and those selected in the shifted grid (bottom panel). The detection statistic threshold is shown in Figure 4.6 as a continuous red line and is not surpassed by any of the candidates. The detection statistic values distribution across the explored frequency range is not uniform due to the presence of noise artifacts (see e.g., the triple peak in the range $89 - 90$Hz) and to the globally non-flat detector noise curve, which decreases as the frequency increases. Unfortunately, none of the candidates is loud enough to overcome the threshold, thus, upper limits on the strain of the signal are computed, as shown in the next section.
Moreover, it is interesting to take a look at the candidate distribution in the parameter space of $(f, \dot{f})$ and (A, B), as shown respectively in Figures 4.7 and 4.8. These representations are helpful to visualize the regions defined from Equations (4.4) and

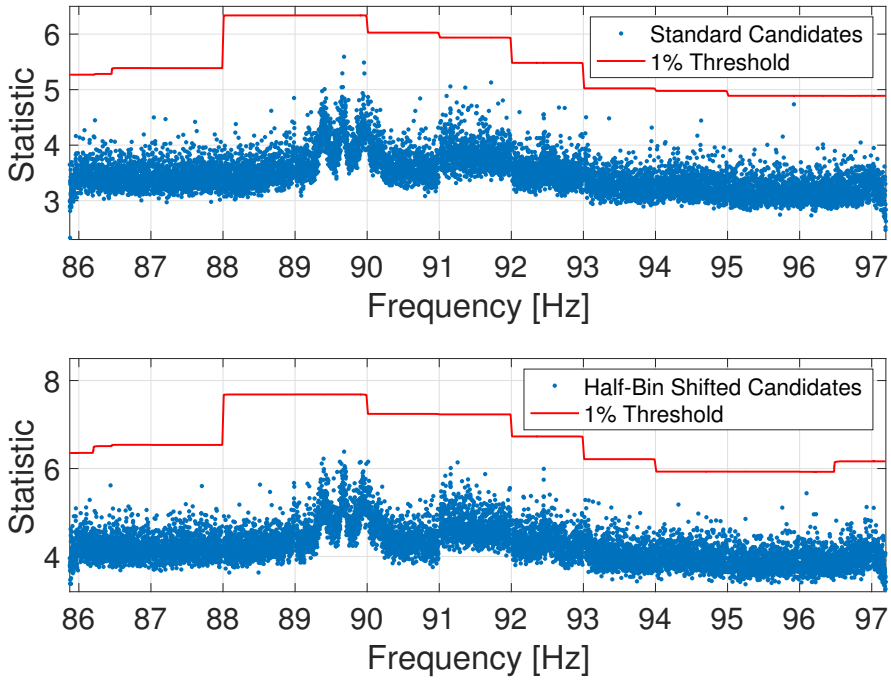

Figure 4.6. Normalized detection statistic for candidates selected in the natural frequency grid after the application of the vetoing criteria discussed in the text. The top panel refers to the natural frequency grid, while the bottom panel refers to the shifted frequency grid. The red continuous line represents the 1% p-value threshold on the detection statistic used to identify significant candidates.

(4.5), which are a rectangle for the physical parameters (A, B) and a parallelogram for $(f, \dot{f})$. In addition the effect of the application of the first veto is highlighted in the panels in Fig. 4.7.

4.6 Upper Limits

In this Section, I will firstly describe how the upper limits on the signal strain amplitude can be computed in Sec. 4.6.1. Then, in Sec. 4.6.2, I will present the results obtained for this search.

4.6.1 Estimation Method

Upper limits at 90% confidence level are computed every 0.25Hz by means of software injections based on the procedure already used in standard *narrow-band* searches (see, e.g., [45, 60, 22]). Specifically, for each 0.25Hz band, sets of 240 signals, with a fixed amplitude and randomly chosen parameters in their allowed range of variation, are injected in O3 data. The signal frequency and spin-down rate are shifted at each glitch epoch in such a way as to simulate glitches that occurred in the real signal we are searching for. This operation is performed by randomly selecting a couple of

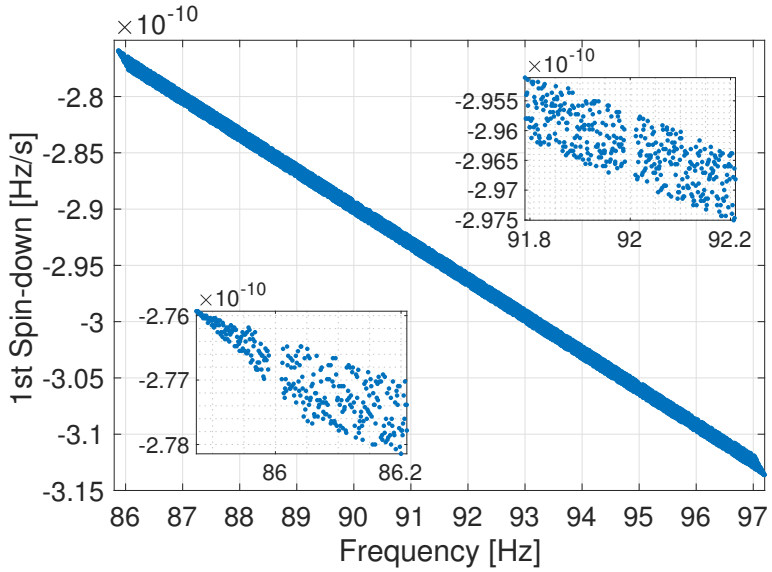

Figure 4.7. Candidates in the frequency/spin-down space after vetoing criteria have been applied. In the two insets, we highlight the 0.02 Hz gaps around the integer frequencies (due to the presence of detector disturbances) and the shape of the regions at the edges. This shape is constrained from Equations 4.4 and 4.5.

parameters A and B corresponding to the interested range and then by computing the values of f and $\dot{f}$ in the different periods.
These data are analyzed exactly in the same way as in the real search and the number of detected signals (i.e., those producing a value of the detection statistic above the detection threshold $\mathcal{S}_{\rm thr}$) is registered. By repeating the procedure for different amplitudes, the value corresponding to a detection efficiency of 90% is obtained through a linear interpolation among the two amplitudes corresponding to a detection probability just below and above 90%, respectively. An example of this procedure for the band $[93, 93.25]$Hz is shown in Figure 4.9. It is also possible to find the situations represented in Figures 4.10 and 4.11, which are the cases respectively of the bands $[92, 92.25]$Hz and $[91.5, 91.75]$Hz. In these cases, we have one or more points corresponding exactly to the value of the detection statistic. In the first case, the upper limit is simply set to the found point, while, in the second case, an average on the corresponding values of $\mathcal{S}$ is performed.

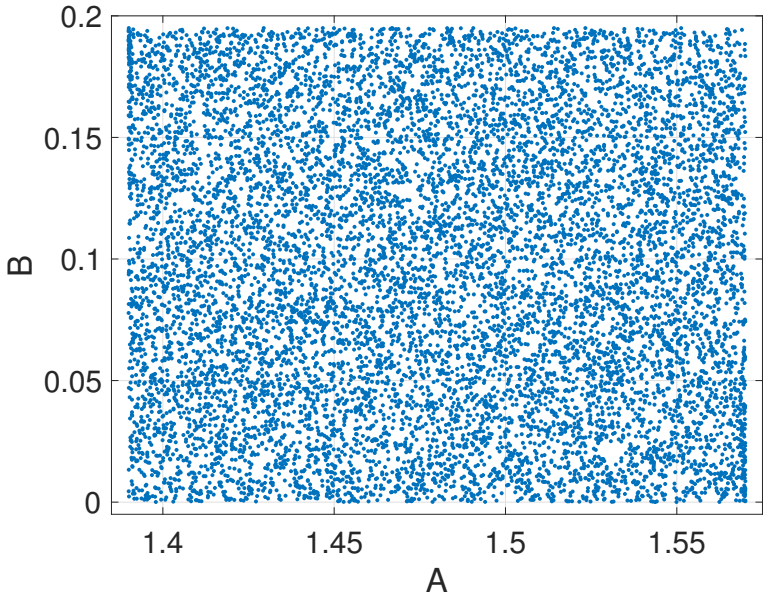

Figure 4.8. Candidates in the space of physical parameters (A, B) after vetoing criteria have been applied.

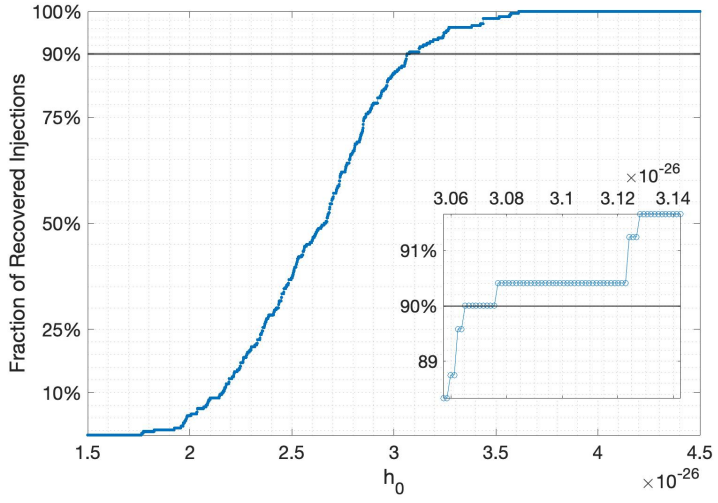

Figure 4.11. Fraction of recovered injected signals as a function of the strain amplitude h_0. In this case there are multiple values of h_0 corresponding to the 90% threshold: the upper limit is computed as the average of these values. This example refers to the band $[91.5, 91.75]$Hz.

4.6.2 Strain Amplitude Upper Limits

The upper limits on the GW strain amplitude h_0 obtained using the previously described method are shown in Figure 4.12. The lower blue curve is obtained assuming a uniform prior on the polarization angle ψ and on the cosine of the star's

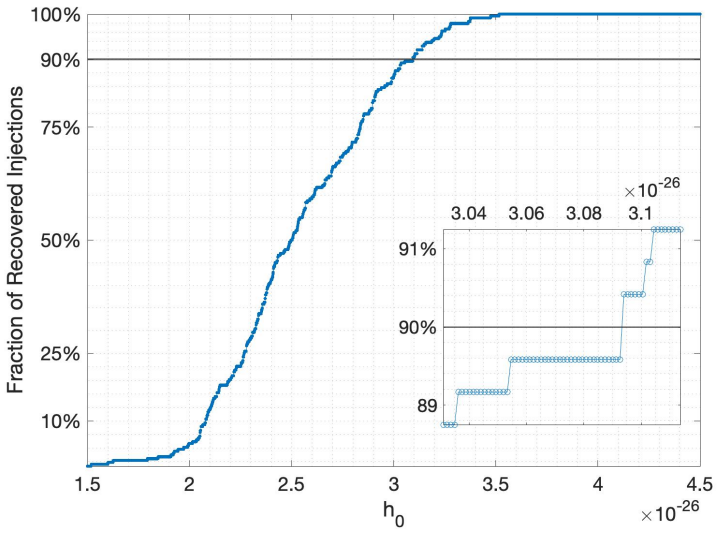

Figure 4.9. Fraction of recovered injected signals as a function of the strain amplitude h_0. The 90% threshold represents the level where the upper limit is identified. On the bottom-right corner, we show an enlargement of the upper limit region. This example refers to the band $[93, 93.25]$Hz.

spin axis inclination angle ι (which correspond to an unknown orientation for the pulsar).

On the other hand, the upper red curve assumes a "restricted" prior on ψ and ι, based on X-ray observations of the pulsar wind nebula, as discussed in Section 4.2. Specifically, we use for ψ a Gaussian distribution centered at 2.2864 rad with width of 0.0384 rad and a double Gaussian distribution for ι centered at 1.522 rad and at 1.620 rad, both with standard deviation 0.016 rad.

Signals injected in data are modeled using the narrow-band expression in (2.6), thus the changing amplitude is the parameter H_0, which should be converted in terms of the strain amplitude h_0 of the standard formalism (2.3). The conversion expression has been provided in Eq. (2.10): this is the point where the assumed distribution for ι affects the result. On the other hand, the distribution for ψ directly affects the signal model through the complex amplitudes $H_{+/\times}$. The uncertainty on the upper limit is given by the combination in quadrature of the statistical error due to the finite number of injections ($\sim 6\%$), the interpolation error in computing the amplitude corresponding to a detection efficiency of 90% (less than $\sim 1\%$), and the data calibration uncertainty ($\sim 7\%$) (see Section 4.1). It is possible to see that the upper limits obtained using the "restricted" prior are higher (worse) than those obtained with uniform prior. This result is counter-intuitive, but is explained by the fact that, since the inclination angle ι is close to $\pi/2$, the GW signal is almost linearly polarized. Thus, it has nearly the smallest maximum signal-to-noise ratio achievable.

From the numerical values of the upper limits, it is clear that the sensitivity of the search is increased of a factor ~ 3 with respect to the results obtained in [4] for the O1 and O2 runs. The reader should also remind that, in those cases it was not

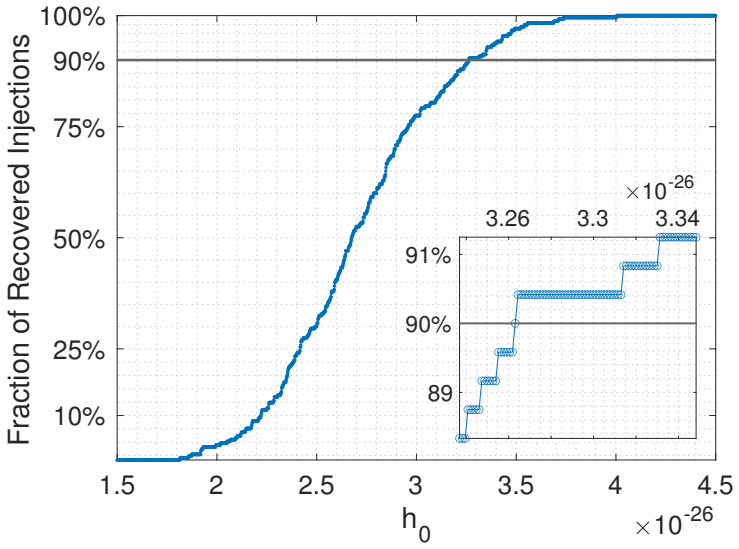

Figure 4.10. Fraction of recovered injected signals as a function of the strain amplitude h_0. In this case there is a single value of h_0 corresponding to the 90% threshold. This value is exactly the upper limit This example refers to the band $[92, 92.25]$Hz.

possible to known when glitches occurred.

4.7 Astrophysical Constraints

In this Section, I will discuss the astrophysical consequences of the obtained results. The main goal is to understand if we are probing a realistic portion of parameter space and if we are able to constrain theoretical models for r-mode driven spin-down of PSR J0537-6910. For this reason, I will compare the obtained upper limits on the amplitude to the spin-down upper limit, i.e., the GW amplitude that would be needed to explain the entire measured spin-down of the star, as explained in Sec. 1.3. Accordingly with Eq. (1.35), the spin-down upper limit $h_{\rm sd}$ can be expressed as [11] :

$$h_{\rm sd} = \frac{1}{r}\sqrt{\frac{10G}{c^3}I_3\frac{\nu|\dot{\nu}|}{f^2}} \approx 4.0\times10^{-26}\left(\frac{90\ \text{Hz}}{f}\right), \tag{4.10}$$

where r is distance to the source. The second step has been obtained by assuming $I_3 = 10^{45}$ g $\cdot$ cm^2 and values appropriate for PSR J0537-6910. The spin axis of the star is taken to be in the z direction, and I_{zz} is the moment of inertia. It is important to notice that, in our case, the spin-down limit is not only an upper limit, but it is exactly the predicted amplitude of the signal in the theoretical picture proposed by [3] to explain the observed *inter-glitch* braking index of $n = 7$. There is, however, an uncertainty associated with equation (4.10), as the relation between f, ν, and I_{zz} depends on the unknown Equation of State (EoS) of dense matter. Using the considerations outlined in [30, 5], it is possible to estimate a plausible range for the curve $h_{\rm sd}$ as a function of the frequency, depending only on one parameter, which we can take to be the mass of the star M or I_{zz}, depending on which is more

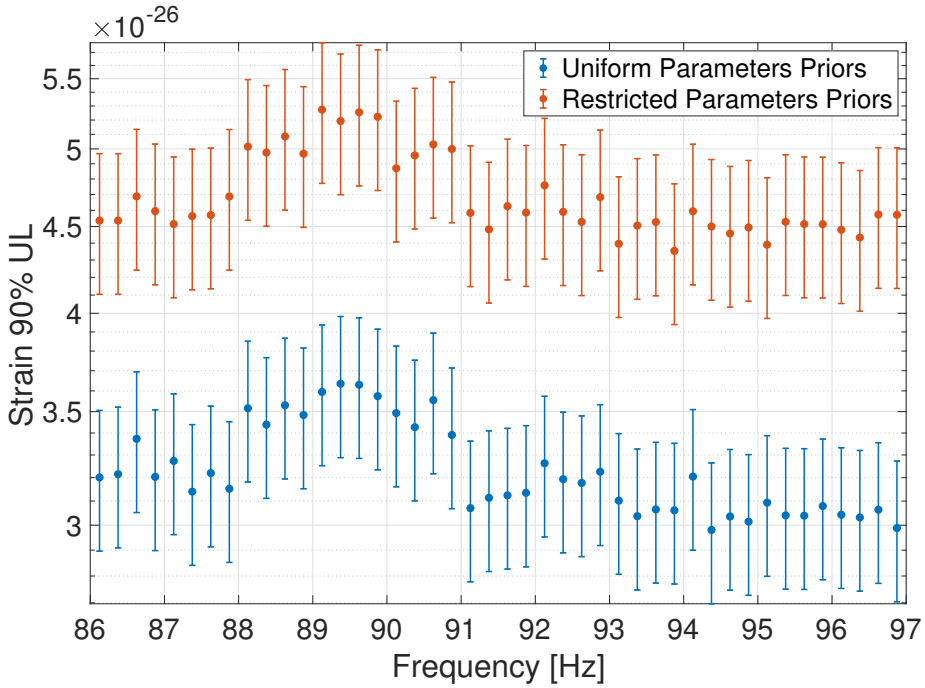

Figure 4.12. GW strain 90% confidence level upper limits as a function of frequency. Bottom blue curve corresponds to uniform prior on the polarization angle ψ and the cosine of the star's rotation axis inclination angle ι, while the upper red curve corresponds to "restricted" priors based on X-ray observations of the pulsar wind nebula [58] .

convenient. The upper limit for this range is set by the stiffest possible EoS from [61], which is causally limited in the core and attached to a realistic crustal model, and the lower limit is set by the softest EoS we consider, called WFF1, that is still compatible with the observations of a $\approx 2M_\odot$ neutron star, as described in [30]. Thus, it is possible to calculate the range of $h_{\rm sd}$ from equation (4.10) and compare it to the sensitivity upper limits of our searches. This is reported in Figure 4.13, where for simplicity only a range between the upper limit set by the stiffest EoS (the causally limited EoS with crust) and the lower limits set by our softest EoS (WFF1) is plotted. It is clear that our searches are probing a physically significant portion of parameter space for all frequencies. Moreover, for frequencies above $f \gtrsim 90$ Hz, our searches are starting to probe below the limits of the r-mode driven spin-down scenario, even in the case of restricted priors.

Another physical quantity of interest is the r-mode amplitude α, already mentioned in Sec. 1.3. By combining Eq.uations (4.10) and (1.34), it is possible to express α in terms of the GW signal amplitude:

$$\alpha = \sqrt{\frac{5}{8\pi}}\frac{c^5}{G}\frac{h_0}{(2\pi f)^3}\frac{d}{MR^3\tilde{J}} \approx 0.017\left(\frac{90\ \text{Hz}}{f}\right)^3\left(\frac{h_0}{10^{-26}}\right), \tag{4.11}$$

where for the second step typical values of $M = 1.4\,M_\odot$ and $R = 12$ km are used. $\tilde{J}$ is the dimensionless canonical angular momentum of the r-mode, which depends only weakly on the EoS. Accordingly to [39], it is possible to fix to $\tilde{J} = 0.0164$ for an $n = 1$ polytrope. Eq. (4.11) can then be used in order to translate the

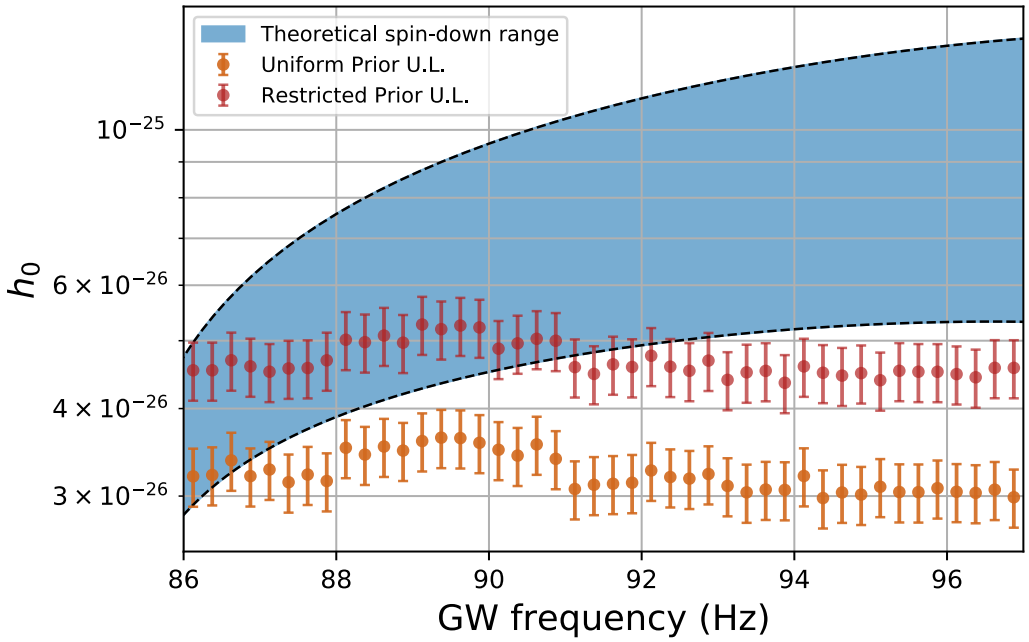

Figure 4.13. Upper limits on GW amplitude $h_0(f)$ obtained from the searches compared to the r ange obtained for the spin-down limit. The dashed lines are set by the stiffest and softest EoSs considered here. **Credit: B. Haskell.**

upper limits in terms of α. The comparison between the spin-down upper limits on the amplitude α for the two limiting EoSs and the results obtained from the search is reported in Fig.4.14. The search upper limits are reported in terms of an observational range., which accounts for the uncertainty on the upper limits. The sensitivity of the searches is close to or below the spin-down limit, especially for the stiffest EoS, and it is starting to constrain the range of values predicted by theoretical models such as those of [3, 62].

4.7.1 Constraints on the Pulsar Mass

As described in [5], it is also possible to express the constraints on the r-mode driven spin-down scenario in terms of a constraint on the mass of the neutron star. This result can be obtained by using the EoS-independent relations between moment of inertia and compactness in [63], together with the fits of [30], so that the only free parameter that encodes the EoS dependence in Eq.(4.10) is the mass of the star. The results are plotted in Figure 4.15. It is possible to see that the observational results do not exclude the case of an r-mode driven spin-down scenario for soft EoSs and lower-mass neutron stars. However, most of the parameter space is actually excluded, and only the softest EoSs and neutron star masses $M \lesssim 0.9 M_\odot$ are consistent with a GW driven spin-down.

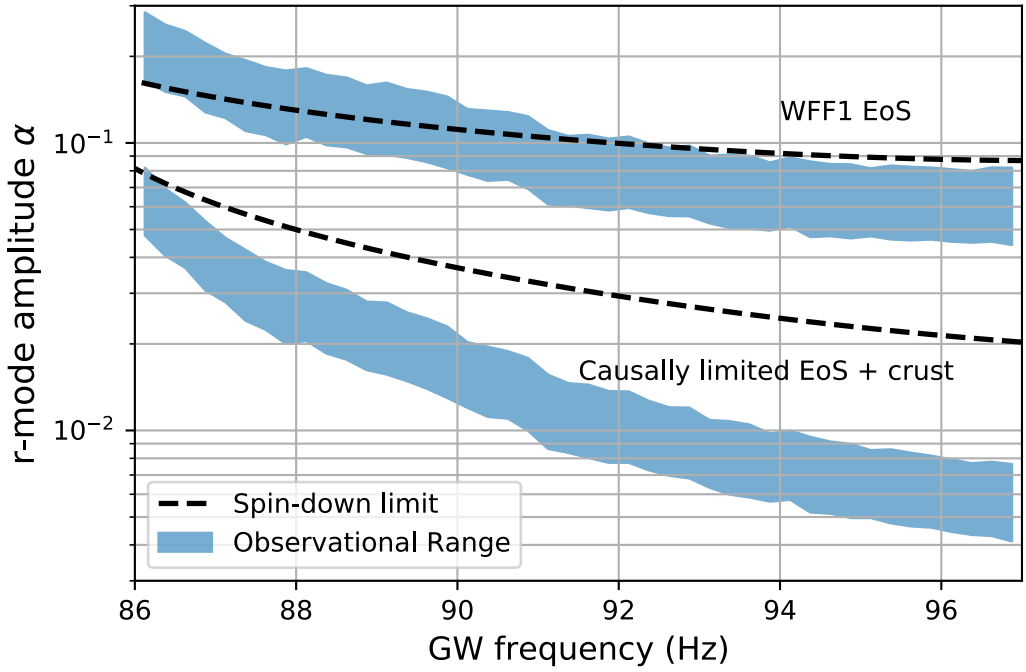

Figure 4.14. Upper limits on the r-mode amplitude α calculated for two different EoSs. The dotted lines show the amplitude α that would correspond to the spin-down limit. In this case, the search upper limits are reported as a range, differently from before. **Credit: B. Haskell.**

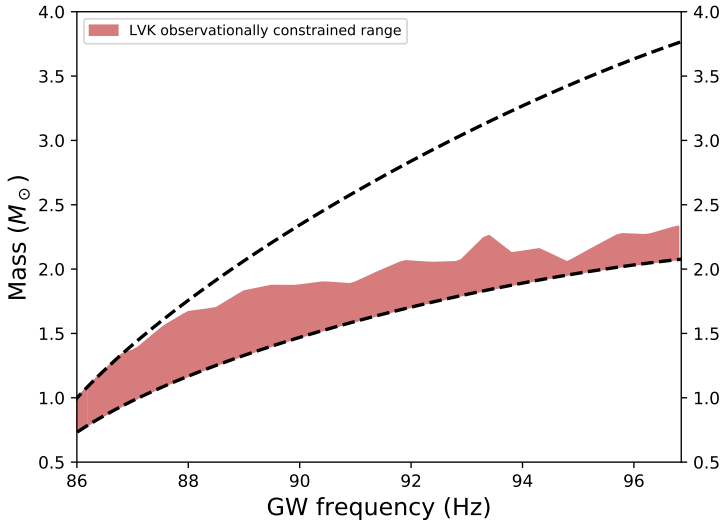

Figure 4.15. Limits on the mass M of PSR J0537-6910 which is consistent with the assumption that gravitational-wave emission due to r-modes is the dominant mechanism causing the observed spin-down behavior of the pulsar. Dashed lines represent the limits provided by the stiffest and the softest EoSs used for these considerations (see text for details). **Credit: B. Haskell.**

Conclusions

I have begun this dissertation by presenting the characteristics of r-modes oscillations and the coupled GW emission. Then, I have presented the narrow-band *5-vectors* pipeline, which I have extended in order to perform searches for r-mode GWs. Finally, I have discussed the search for r-modes gravitational emission from the X-ray pulsar PSR J0537-6910, which is motivated by theoretical models and observational evidence that the spin-down of the pulsar may be driven by GW emission due to such an unstable oscillation. The search is enabled by a timing ephemeris obtained from *NICER* telescope data [40], which includes the times of three *glitches*, and allows us to search in the LIGO-Virgo O3 run data-taking time spans between *glitches*, making use of the narrow-band pipeline based on the *5-vectors* method.
Unfortunately, no signal has been detected, but it was possible to set upper limits on the GW strain amplitude, which improve by a factor of up to 3 on previous upper limits obtained in [4], which uses data from the O1 and O2 runs of the Advanced LIGO network. The improvement is mostly due to the increased sensitivity of the O3 data analyzed in our searches and to the contemporaneous timing ephemeris obtained from *NICER* data, but an important add-on of this search is the possibility to precisely account for *glitch* occurrences.
The upper limits set by this search probe a significant portion of parameter space for all frequencies and are beginning to be in tension with the lower limits predicted for the strain if GW emission due to r-modes is indeed driving the entire spin-down of PSR J0537-6910, as an *inter-glitch* braking index $n \approx 7$ (obtained by *NICER*) would suggest. In fact, only a neutron star with mass $M \lesssim 0.9 M_{\odot}$ is still consistent with the star being spun down only by GW emission due to r-modes.
In other words, for a range of frequencies $f \gtrsim 90$ Hz, our searches are probing below the spin-down limit, and would be sensitive to emission due to r-modes of lower amplitude than that needed to explain the observations of an *inter-glitch* braking index of $n = 7$ or to the presence of an r-mode that is excited by the *glitch* but subsequently damped. In the case in which the r-mode is damped, the sensitivity of the search will be degraded, as discussed in detail in [4], which reports a degradation by a factor of ≈ 4 with respect to the case where the mode is always on.
The important results obtained allow us to conclude that it is fundamental to continue along the direction of this search: an eventual detection would be of great theoretical importance, as it would be the first direct detection of GW emission due to r-modes, providing us insights on the physics of pulsars matter. The developed pipeline can be easily used for future searches of this kind and it can be easily generalized in order to be applied in similar situations.

Bibliography

[1] Albert Einstein. "Näherungsweise Integration Der Feldgleichungen Der Gravitation". In: *Sitzungsberichte der Königlich Preußischen Akademie der Wissenschaften (Berlin), Seite 688-696.* (1916).

[2] LIGO Scientific Collaboration and Virgo Collaboration et al. "Observation of Gravitational Waves from a Binary Black Hole Merger". In: *Physical Review Letters* 116.6 (Feb. 2016), p. 061102. DOI: 10.1103/PhysRevLett.116.061102.

[3] N. Andersson et al. "The Enigmatic Spin Evolution of PSR J0537–6910: R-Modes, Gravitational Waves, and the Case for Continued Timing". en. In: *The Astrophysical Journal* 864.2 (Sept. 2018), p. 137. ISSN: 1538-4357. DOI: 10.3847/1538-4357/aad6eb.

[4] Liudmila Fesik and Maria Alessandra Papa. "First Search for R-Mode Gravitational Waves from PSR J0537–6910". en. In: *The Astrophysical Journal* 895.1 (May 2020), p. 11. ISSN: 0004-637X. DOI: 10.3847/1538-4357/ab8193.

[5] The LIGO Scientific Collaboration et al. "Constraints from LIGO O3 Data on Gravitational-Wave Emission Due to r-Modes in the Glitching Pulsar PSR J0537-6910". In: *arXiv:2104.14417 [astro-ph, physics:gr-qc]* (Apr. 2021). arXiv: 2104.14417 [astro-ph, physics:gr-qc].

[6] Piotr Jaranowski, Andrzej Królak, and Bernard F. Schutz. "Data Analysis of Gravitational-Wave Signals from Spinning Neutron Stars: The Signal and Its Detection". In: *Physical Review D* 58.6 (Aug. 1998), p. 063001. DOI: 10.1103/PhysRevD.58.063001.

[7] Nils Andersson and Kostas D. Kokkotas. "The R-Mode Instability in Rotating Neutron Stars". In: *International Journal of Modern Physics D* 10 (2001), pp. 381–441. ISSN: 0218-2718. DOI: 10.1142/S0218271801001062.

[8] Brynmor Haskell. "R-Modes in Neutron Stars: Theory and Observations". en. In: *International Journal of Modern Physics E* 24.09 (Sept. 2015), p. 1541007. ISSN: 0218-3013, 1793-6608. DOI: 10.1142/S0218301315410074. arXiv: 1509.04370.

[9] Kostas D. Kokkotas and Kai Schwenzer. "R-Mode Astronomy". en. In: *The European Physical Journal A* 52.2 (Feb. 2016), p. 38. ISSN: 1434-6001, 1434-601X. DOI: 10.1140/epja/i2016-16038-9.

[10] Valeria Ferrari, Leonardo Gualtieri, and Paolo Pani. *General Relativity and Its Applications: Black Holes, Compact Stars and Gravitational Waves*. Boca Raton: CRC Press, Dec. 2020. ISBN: 978-0-429-49140-5. DOI: 10.1201/9780429491405.

[11] Benjamin J. Owen. "How to Adapt Broad-Band Gravitational-Wave Searches for r-Modes". en. In: *Physical Review D* 82.10 (Nov. 2010), p. 104002. ISSN: 1550-7998, 1550-2368. DOI: 10.1103/PhysRevD.82.104002. arXiv: 1006.1994.

[12] Santiago Caride et al. "How to Search for Gravitational Waves from R-Modes of Known Pulsars". In: *Physical Review D* 100.6 (Sept. 2019), p. 064013. DOI: 10.1103/PhysRevD.100.064013.

[13] Wynn C. G. Ho et al. "Return of the Big Glitcher: NICER Timing and Glitches of PSR J0537-6910". en. In: *Monthly Notices of the Royal Astronomical Society* 498.4 (Sept. 2020), pp. 4605–4614. ISSN: 0035-8711, 1365-2966. DOI: 10.1093/mnras/staa2640. arXiv: 2009.00030.

[14] J. Papaloizou and J. E. Pringle. "Non-Radial Oscillations of Rotating Stars and Their Relevance to the Short-Period Oscillations of Cataclysmic Variables". In: *Monthly Notices of the Royal Astronomical Society* 182 (Feb. 1978), pp. 423–442. ISSN: 0035-8711. DOI: 10.1093/mnras/182.3.423.

[15] Binod Rajbhandari et al. "First Searches for Gravitational Waves from R-Modes of the Crab Pulsar". en. In: *arXiv:2101.00714 [astro-ph, physics:gr-qc]* (Jan. 2021). arXiv: 2101.00714 [astro-ph, physics:gr-qc].

[16] Nils Andersson. "A New Class of Unstable Modes of Rotating Relativistic Stars". In: *The Astrophysical Journal* 502.2 (Aug. 1998), pp. 708–713. DOI: 10.1086/305919.

[17] John L. Friedman and Sharon M. Morsink. "Axial Instability of Rotating Relativistic Stars". In: *The Astrophysical Journal* 502.2 (Aug. 1998), pp. 714–720. DOI: 10.1086/305920.

[18] K. H. Lockitch, J. L. Friedman, and N. Andersson. "The Rotational Modes of Relativistic Stars: Numerical Results". In: *Physical Review D* 68.12 (Dec. 2003), p. 124010. ISSN: 0556-2821, 1089-4918. DOI: 10.1103/PhysRevD.68.124010. arXiv: gr-qc/0210102.

[19] J. Provost, G. Berthomieu, and A. Rocca. "Low Frequency Oscillations of a Slowly Rotating Star - Quasi Toroidal Modes". In: *Astronomy and Astrophysics* 94 (Jan. 1981), p. 126. ISSN: 0004-6361.

[20] Kip S. Thorne. "Multipole Expansions of Gravitational Radiation". In: *Reviews of Modern Physics* 52.2 (Apr. 1980), pp. 299–339. DOI: 10.1103/RevModPhys.52.299.

[21] Michele Maggiore. "Gravitational Waves. Volume 1: Theory and Experiments". In: *General relativity and gravitation* 41.7 (2008), pp. 1667–1669. ISSN: 0001-7701. DOI: 10.1007/s10714-009-0762-5.

[22] LIGO Scientific Collaboration and Virgo Collaboration et al. "Narrow-Band Search for Gravitational Waves from Known Pulsars Using the Second LIGO Observing Run". In: *Physical Review D* 99.12 (June 2019), p. 122002. DOI: 10.1103/PhysRevD.99.122002.

[23] The LIGO Scientific Collaboration et al. "First Search for Gravitational Waves from Known Pulsars with Advanced LIGO". In: *The Astrophysical Journal* 839.1 (Apr. 2017). Comment: 19 pages, 4 tables, 4 figures, accepted by The Astrophysical Journal. Fixes Equation 4. Science summary of results available at http://www.ligo.org/science/Publication-O1KnownPulsar/index.php, p. 12. ISSN: 1538-4357. DOI: 10.3847/1538-4357/aa677f. arXiv: 1701.07709.

[24] R. Abbott et al. "Diving below the Spin-down Limit: Constraints on Gravitational Waves from the Energetic Young Pulsar PSR J0537-6910". en. In: *The Astrophysical Journal Letters* 913.2 (May 2021), p. L27. ISSN: 2041-8205. DOI: 10.3847/2041-8213/abffcd.

[25] J. L. Friedman and B. F. Schutz. "Secular Instability of Rotating Newtonian Stars". In: *The Astrophysical Journal* 222 (May 1978), pp. 281–296. ISSN: 0004-637X. DOI: 10.1086/156143.

[26] Kostas Glampedakis and Leonardo Gualtieri. "Gravitational Waves from Single Neutron Stars: An Advanced Detector Era Survey". en. In: *arXiv:1709.07049 [astro-ph, physics:gr-qc]* 457 (2018). Comment: 39 pages, 12 figures, 2 tables. Chapter of the book "Physics and Astrophysics of Neutron Stars", NewCompStar COST Action 1304. Minor corrections to match published version, pp. 673–736. DOI: 10.1007/978-3-319-97616-7_12. arXiv: 1709.07049 [astro-ph, physics:gr-qc].

[27] Yuri Levin and Greg Ushomirsky. "Crust-Core Coupling and r-Mode Damping in Neutron Stars: A Toy Model". en. In: *Monthly Notices of the Royal Astronomical Society* 324.4 (July 2001), pp. 917–922. ISSN: 00358711, 13652966. DOI: 10.1046/j.1365-8711.2001.04323.x.

[28] Vasileios Paschalidis and Nikolaos Stergioulas. "Rotating Stars in Relativity". In: *Living Reviews in Relativity* 20.1 (Dec. 2017). Comment: 174 pages, 40 figures, accepted by Living Reviews in Relativity, matches published version, p. 7. ISSN: 2367-3613, 1433-8351. DOI: 10.1007/s41114-017-0008-x. arXiv: 1612.03050.

[29] Shijun Yoshida, Shin'ichirou Yoshida, and Yoshiharu Eriguchi. "R-Mode Oscillations of Rapidly Rotating Barotropic Stars in General Relativity: Analysis by the Relativistic Cowling Approximation". In: *Monthly Notices of the Royal Astronomical Society* 356.1 (Jan. 2005). Comment: 9 pages, 6 figures, pp. 217–224. ISSN: 0035-8711, 1365-2966. DOI: 10.1111/j.1365-2966.2004.08436.x. arXiv: astro-ph/0406283.

[30] Ashikuzzaman Idrisy, Benjamin J. Owen, and David I. Jones. "R-Mode Frequencies of Slowly Rotating Relativistic Neutron Stars with Realistic Equations of State". In: *Physical Review D* 91.2 (Jan. 2015). Comment: 16 pages, 5 figures, p. 024001. ISSN: 1550-7998, 1550-2368. DOI: 10.1103/PhysRevD.91.024001. arXiv: 1410.7360.

[31] Jason W. T. Hessels et al. “A Radio Pulsar Spinning at 716 Hz”. en. In: *Science* 311.5769 (Mar. 2006), pp. 1901–1904. ISSN: 0036-8075, 1095-9203. DOI: 10.1126/science.1123430.

[32] Feryal Ozel and Paulo Freire. “Masses, Radii, and Equation of State of Neutron Stars”. In: *Annual Review of Astronomy and Astrophysics* 54.1 (Sept. 2016). Comment: To be published in Annual Reviews of Astronomy and Astrophysics 2016. All mass, radius, and equation of state data are available at http://xtreme.as.arizona.edu/NeutronStars, pp. 401–440. ISSN: 0066-4146, 1545-4282. DOI: 10.1146/annurev-astro-081915-023322. arXiv: 1603.02698.

[33] P. W. Anderson and N. Itoh. “Pulsar Glitches and Restlessness as a Hard Superfluidity Phenomenon”. en. In: *Nature* 256.5512 (July 1975), pp. 25–27. ISSN: 1476-4687. DOI: 10.1038/256025a0.

[34] M. A. Alpar et al. “Vortex Creep and the Internal Temperature of Neutron Stars. I - General Theory”. en. In: *The Astrophysical Journal* 276 (Jan. 1984), pp. 325–334. ISSN: 0004-637X. DOI: 10.1086/161616.

[35] R. D. Ferdman et al. “The Glitches and Rotational History of the Highly Energetic Young Pulsar PSR J0537-6910”. In: *The Astrophysical Journal* 852 (Jan. 2018), p. 123. ISSN: 0004-637X. DOI: 10.3847/1538-4357/aaa198.

[36] Wynn C. G. Ho. “Magnetic Field Growth in Young Glitching Pulsars with a Braking Index”. In: *Monthly Notices of the Royal Astronomical Society* 452.1 (Sept. 2015), pp. 845–851. ISSN: 0035-8711. DOI: 10.1093/mnras/stv1339.

[37] C. M. Espinoza, A. G. Lyne, and B. W. Stappers. “New Long-Term Braking Index Measurements for Glitching Pulsars Using a Glitch-Template Method”. In: *Monthly Notices of the Royal Astronomical Society* 466.1 (Apr. 2017), pp. 147–162. ISSN: 0035-8711. DOI: 10.1093/mnras/stw3081.

[38] Stuart L. Shapiro and Saul A. Teukolsky. “Black Holes, White Dwarfs, and Neutron Stars: The Physics of Compact Objects”. In: *Research supported by the National Science Foundation. New York, Wiley-Interscience, 1983, 663 p.* (1983).

[39] Benjamin J. Owen et al. “Gravitational Waves from Hot Young Rapidly Rotating Neutron Stars”. In: *Physical Review D* 58 (Oct. 1998), p. 084020. ISSN: 1550-7998. DOI: 10.1103/PhysRevD.58.084020.

[40] Wynn C. G. Ho and Nils Andersson. “Rotational Evolution of Young Pulsars Due to Superfluid Decoupling”. en. In: *Nature Physics* 8.11 (Nov. 2012), pp. 787–789. ISSN: 1745-2481. DOI: 10.1038/nphys2424.

[41] J. Middleditch et al. “Predicting the Starquakes in PSR J0537-6910”. In: *The Astrophysical Journal* 652 (Dec. 2006), pp. 1531–1546. ISSN: 0004-637X. DOI: 10.1086/508736.

[42] A. G. Lyne et al. “45 Years of Rotation of the Crab Pulsar”. In: *Monthly Notices of the Royal Astronomical Society* 446 (Jan. 2015), pp. 857–864. ISSN: 0035-8711. DOI: 10.1093/mnras/stu2118.

[43] Simon Johnston and A. Karastergiou. “Pulsar Braking and the P–P’ Diagram”. In: *Monthly Notices of the Royal Astronomical Society* 467.3 (June 2017), pp. 3493–3499. ISSN: 0035-8711. DOI: 10.1093/mnras/stx377.

[44] Roger W. Romani. “A Unified Model of Neutron-Star Magnetic Fields”. en. In: *Nature* 347.6295 (Oct. 1990), pp. 741–743. ISSN: 1476-4687. DOI: 10.1038/347741a0.

[45] Simone Mastrogiovanni. “Advanced Data Analysis Techniques for the Detection of Gravitational Waves from Asymmetric Spinning Neutron Stars: An Application to the First and Second LIGO-Virgo Observing Runs”. PhD Thesis. mastrosi@apc.in2p3.fr: Sapienza - Tor Vergata, Oct. 2018.

[46] P Astone et al. “A Method for Detection of Known Sources of Continuous Gravitational Wave Signals in Non-Stationary Data”. en. In: *Classical and Quantum Gravity* 27.19 (Oct. 2010), p. 194016. ISSN: 0264-9381, 1361-6382. DOI: 10.1088/0264-9381/27/19/194016.

[47] P. Astone et al. “Method for Narrow-Band Search of Continuous Gravitational Wave Signals”. en. In: *Physical Review D* 89.6 (Mar. 2014), p. 062008. ISSN: 1550-7998, 1550-2368. DOI: 10.1103/PhysRevD.89.062008.

[48] S Mastrogiovanni et al. “An Improved Algorithm for Narrow-Band Searches of Continuous Gravitational Waves”. en. In: *Classical and Quantum Gravity* 34.13 (July 2017), p. 135007. ISSN: 0264-9381, 1361-6382. DOI: 10.1088/1361-6382/aa744f.

[49] J. Abadie et al. “Beating the Spin-Down Limit on Gravitational Wave Emission from the Vela Pulsar”. en. In: *The Astrophysical Journal* 737.2 (Aug. 2011), p. 93. ISSN: 0004-637X, 1538-4357. DOI: 10.1088/0004-637X/737/2/93.

[50] T. Accadia et al. “The NoEMi (Noise Frequency Event Miner) Framework”. en. In: *Journal of Physics: Conference Series* 363 (June 2012), p. 012037. ISSN: 1742-6596. DOI: 10.1088/1742-6596/363/1/012037.

[51] T. Accadia et al. “Noise Monitor Tools and Their Application to Virgo Data”. en. In: *Journal of Physics: Conference Series* 363 (June 2012), p. 012024. ISSN: 1742-6596. DOI: 10.1088/1742-6596/363/1/012024.

[52] P Astone, S Frasca, and C Palomba. “The Short FFT Database and the Peak Map for the Hierarchical Search of Periodic Sources”. en. In: *Classical and Quantum Gravity* 22.18 (Sept. 2005), S1197–S1210. ISSN: 0264-9381, 1361-6382. DOI: 10.1088/0264-9381/22/18/S34.

[53] A. W. Irwin and T. Fukushima. “A Numerical Time Ephemeris of the Earth”. en. In: *Astronomy and Astrophysics* 348 (Aug. 1999), pp. 642–652. ISSN: 0004-6361.

[54] and J. Aasi et al. “Advanced LIGO”. en. In: *Classical and Quantum Gravity* 32.7 (Mar. 2015), p. 074001. ISSN: 0264-9381. DOI: 10.1088/0264-9381/32/7/074001.

[55] Catherine Nguyen. "Status of the Advanced Virgo Gravitational-Wave Detector". In: *arXiv:2105.09247 [astro-ph]* (May 2021). Comment: 8 pages, 8 figures, Proceedings of Theory meeting experiments (TMEX 2020), 16th Rencontres du Vietnam. arXiv: 2105.09247 [astro-ph].

[56] Ling Sun et al. "Characterization of Systematic Error in Advanced LIGO Calibration". en. In: *Classical and Quantum Gravity* 37.22 (Oct. 2020), p. 225008. ISSN: 0264-9381. DOI: 10.1088/1361-6382/abb14e.

[57] Leisa K. Townsley et al. "A *Chandra* ACIS Study of 30 Doradus. II. X-Ray Point Sources in the Massive Star Cluster R136 and Beyond". en. In: *The Astronomical Journal* 131.4 (Apr. 2006), pp. 2164–2184. ISSN: 0004-6256, 1538-3881. DOI: 10.1086/500535.

[58] C.-Y. Ng and Roger W. Romani. "Fitting Pulsar Wind Tori. II. Error Analysis and Applications". en. In: *The Astrophysical Journal* 673.1 (Jan. 2008), pp. 411–417. ISSN: 0004-637X, 1538-4357. DOI: 10.1086/523935.

[59] D. I. Jones. "Gravitational Wave Emission from Rotating Superfluid Neutron Stars". en. In: *Monthly Notices of the Royal Astronomical Society* 402.4 (Mar. 2010), pp. 2503–2519. ISSN: 00358711, 13652966. DOI: 10.1111/j.1365-2966.2009.16059.x.

[60] B. P. Abbott et al. "First Narrow-Band Search for Continuous Gravitational Waves from Known Pulsars in Advanced Detector Data". In: *Physical Review D* 96.12 (Dec. 2017), p. 122006. DOI: 10.1103/PhysRevD.96.122006.

[61] B. Haskell et al. "Fundamental Physics and the Absence of Sub-Millisecond Pulsars". In: *Astronomy & Astrophysics* 620 (Dec. 2018). Comment: Submitted to A&A, A69. ISSN: 0004-6361, 1432-0746. DOI: 10.1051/0004-6361/201833521. arXiv: 1805.11277.

[62] Mark G. Alford and Kai Schwenzer. "Gravitational Wave Emission and Spin-Down of Young Pulsars". en. In: *The Astrophysical Journal* 781.1 (Jan. 2014), p. 26. ISSN: 0004-637X, 1538-4357. DOI: 10.1088/0004-637X/781/1/26.

[63] Cosima Breu and Luciano Rezzolla. "Maximum Mass, Moment of Inertia and Compactness of Relativistic Stars". en. In: *Monthly Notices of the Royal Astronomical Society* 459.1 (June 2016), pp. 646–656. ISSN: 0035-8711, 1365-2966. DOI: 10.1093/mnras/stw575.